Chapter 2
Scanning Probe Microscopy – Principle of Operation, Instrumentation, and Probes

Bharat Bhushan and Othmar Marti

Abstract Since the introduction of the STM in 1981 and the AFM in 1985, many variations of probe-based microscopies, referred to as SPMs, have been developed. While the pure imaging capabilities of SPM techniques initially dominated applications of these methods, the physics of probe–sample interactions and quantitative analyses of tribological, electronic, magnetic, biological, and chemical surfaces using SPMs have become of increasing interest in recent years. SPMs are often associated with nanoscale science and technology, since they allow investigation and manipulation of surfaces down to the atomic scale. As our understanding of the underlying interaction mechanisms has grown, SPMs have increasingly found application in many fields beyond basic research fields. In addition, various derivatives of all these methods have been developed for special applications, some of them intended for areas other than microscopy.

This chapter presents an overview of STM and AFM and various probes (tips) used in these instruments, followed by details on AFM instrumentation and analyses.

The scanning tunneling microscope (STM), developed by Binnig and his colleagues in 1981 at the IBM Zurich Research Laboratory in Rüschlikon (Switzerland), was the first instrument capable of directly obtaining three-dimensional (3-D) images of solid surfaces with atomic resolution [1]. Binnig and Rohrer received a Nobel Prize in Physics in 1986 for their discovery. STMs can only be used to study surfaces which are electrically conductive to some degree. Based on their design of the STM, in 1985, Binnig et al. developed an atomic force microscope (AFM) to measure ultrasmall forces (less than 1 μN) between the AFM tip surface and the sample surface [2] (also see [3]). AFMs can be used to measure any engineering surface, whether it is electrically conductive or insulating. The AFM has become a popular surface profiler for topographic and normal force measurements on the micro- to nanoscale [4]. AFMs modified in order to measure both normal and lateral forces are called lateral force microscopes (LFMs) or friction force microscopes (FFMs) [5, 6, 7, 8, 9, 10, 11]. FFMs have been further modified to measure lateral forces in two orthogonal directions [12, 13, 14, 15, 16]. A number of researchers have modified and improved the original AFM and FFM designs, and have used

B. Bhushan (ed.), *Nanotribology and Nanomechanics*,
DOI 10.1007/978-3-642-15283-2_2,

these improved systems to measure the adhesion and friction of solid and liquid surfaces on micro- and nanoscales [4, 17, 18, 19, 20, 21, 22, 23, 24, 25, 26, 27, 28, 29, 30]. AFMs have been used to study scratching and wear, and to measure elastic/plastic mechanical properties (such as indentation hardness and the modulus of elasticity) [4, 10, 11, 21, 23, 26, 27, 28, 29, 31, 32, 33, 34, 35, 36]. AFMs have been used to manipulate individual atoms of xenon [37], molecules [38], silicon surfaces [39] and polymer surfaces [40]. STMs have been used to create nanofeatures via localized heating or by inducing chemical reactions under the STM tip [41, 42, 43] and through nanomachining [44]. AFMs have also been used for nanofabrication [4, 10, 45, 46, 47] and nanomachining [48].

STMs and AFMs are used at extreme magnifications ranging from 10^3 to 10^9 in the x-, y- and z-directions in order to image macro to atomic dimensions with high resolution and for spectroscopy. These instruments can be used in any environment, such as ambient air [2, 49], various gases [17], liquids [50, 51, 52], vacuum [1, 53], at low temperatures (lower than about 100 K) [54, 55, 56, 57, 58] and at high temperatures [59, 60]. Imaging in liquid allows the study of live biological samples and it also eliminates the capillary forces that are present at the tip–sample interface when imaging aqueous samples in ambient air. Low-temperature (liquid helium temperatures) imaging is useful when studying biological and organic materials and low-temperature phenomena such as superconductivity or charge-density waves. Low-temperature operation is also advantageous for high-sensitivity force mapping due to the reduced thermal vibration. They also have been used to image liquids such as liquid crystals and lubricant molecules on graphite surfaces [61, 62, 63, 64]. While applications of SPM techniques initially focused on their pure imaging capabilities, research into the physics and chemistry of probe–sample interactions and SPM-based quantitative analyses of tribological, electronic, magnetic, biological, and chemical surfaces have become increasingly popular in recent years. Nanoscale science and technology is often tied to the use of SPMs since they allow investigation and manipulation of surfaces down to the atomic scale. As our understanding of the underlying interaction mechanisms has grown, SPMs and their derivatives have found applications in many fields beyond basic research fields and microscopy.

Families of instruments based on STMs and AFMs, called scanning probe microscopes (SPMs), have been developed for various applications of scientific and industrial interest. These include STM, AFM, FFM (or LFM), scanning electrostatic force microscopy (SEFM) [65, 66], scanning force acoustic microscopy (SFAM) (or atomic force acoustic microscopy (AFAM)) [21, 22, 36, 67, 68, 69], scanning magnetic microscopy (SMM) (or magnetic force microscopy (MFM)) [70, 71, 72, 73], scanning near-field optical microscopy (SNOM) [74, 75, 76, 77], scanning thermal microscopy (SThM) [78, 79, 80], scanning electrochemical microscopy (SEcM) [81], scanning Kelvin probe microscopy (SKPM) [82, 83, 84, 85, 86], scanning chemical potential microscopy (SCPM) [79], scanning ion conductance microscopy (SICM) [87, 88] and scanning capacitance microscopy (SCM) [82, 89, 90, 91]. When the technique is used to measure forces (as in AFM, FFM, SEFM, SFAM and SMM) it is also referred to as scanning force microscopy

Table 2.1 Comparison of various conventional microscopes with SPMs

	Optical	SEM/TEM	Confocal	SPM
Magnification	10^3	10^7	10^4	10^9
Instrument price (US$)	$10k	$250k	$30k	$100k
Technology age	200 y	40 y	20 y	20 y
Applications	Ubiquitous	Science and technology	New and unfolding	Cutting edge
Market 1993	$800 M	$400 M	$80 M	$100 M
Growth rate	10%	10%	30%	70%

(SFM). Although these instruments offer atomic resolution and are ideal for basic research, they are also used for cutting-edge industrial applications which do not require atomic resolution. The commercial production of SPMs started with the STM in 1987 and the AFM in 1989 by Digital Instruments, Inc. (Santa Barbara, USA). For comparisons of SPMs with other microscopes, see Table 2.1 (Veeco Instruments, Inc., Santa Barbara, USA). Numbers of these instruments are equally divided between the US, Japan and Europe, with the following split between industry/university and government laboratories: 50/50, 70/30, and 30/70, respectively. It is clear that research and industrial applications of SPMs are expanding rapidly.

2.1 Scanning Tunneling Microscope

The principle of electron tunneling was first proposed by Giaever [93]. He envisioned that if a potential difference is applied to two metals separated by a thin insulating film, a current will flow because of the ability of electrons to penetrate a potential barrier. To be able to measure a tunneling current, the two metals must be spaced no more than 10 nm apart. Binnig et al. [1] introduced vacuum tunneling combined with lateral scanning. The vacuum provides the ideal barrier for tunneling. The lateral scanning allows one to image surfaces with exquisite resolution – laterally to less than 1 nm and vertically to less than 0.1 nm – sufficient to define the position of single atoms. The very high vertical resolution of the STM is obtained because the tunnel current varies exponentially with the distance between the two electrodes; that is, the metal tip and the scanned surface. Typically, the tunneling current decreases by a factor of 2 as the separation is increased by 0.2 nm. Very high lateral resolution depends upon sharp tips. Binnig et al. overcame two key obstacles by damping external vibrations and moving the tunneling probe in close proximity to the sample. Their instrument is called the scanning tunneling microscope (STM). Today's STMs can be used in ambient environments for atomic-scale imaging of surfaces. Excellent reviews on this subject have been presented by Hansma and Tersoff [92], Sarid and Elings [94], Durig et al. [95]; Frommer [96], Güntherodt and Wiesendanger [97], Wiesendanger and Güntherodt [98], Bonnell [99], Marti and Amrein [100], Stroscio and Kaiser [101], and Güntherodt et al. [102].

The principle of the STM is straightforward. A sharp metal tip (one electrode of the tunnel junction) is brought close enough (0.3–1 nm) to the surface to be investigated (the second electrode) to make the tunneling current measurable at a convenient operating voltage (10 mV–1 V). The tunneling current in this case varies from 0.2 to 10 nA. The tip is scanned over the surface at a distance of 0.3–1 nm, while the tunneling current between it and the surface is measured. The STM can be operated in either the constant current mode or the constant height mode (Fig. 2.1). The left-hand column of Fig. 2.1 shows the basic constant current mode of operation. A feedback network changes the height of the tip z to keep the current constant. The displacement of the tip, given by the voltage applied to the piezoelectric drive, then yields a topographic map of the surface. Alternatively, in the constant height mode, a metal tip can be scanned across a surface at nearly constant height and constant voltage while the current is monitored, as shown in the right-hand column of Fig. 2.1. In this case, the feedback network responds just rapidly enough to keep the average current constant. The current mode is generally used for atomic-scale images; this mode is not practical for rough surfaces. A three-dimensional picture $[z(x, y)]$ of a surface consists of multiple scans $[z(x)]$ displayed laterally to each other in the y-direction. It should be noted that if different atomic species are present in a sample, the different atomic species within a sample may produce different tunneling currents for a given bias voltage. Thus the height data may not be a direct representation of the topography of the surface of the sample.

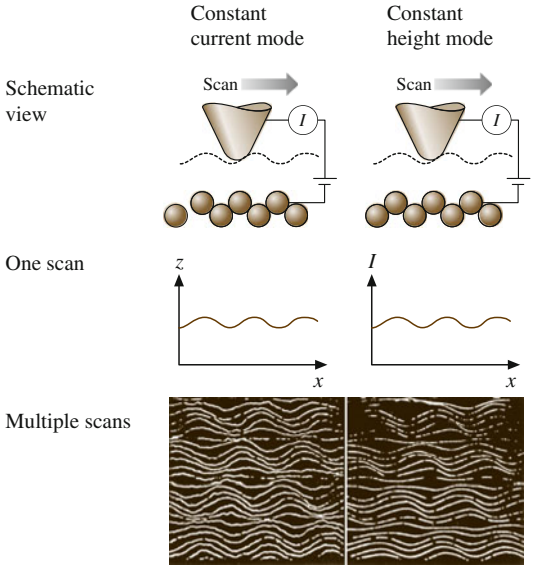

Fig. 2.1 An STM can be operated in either the constant-current or the constant-height mode. The images are of graphite in air (After [92])

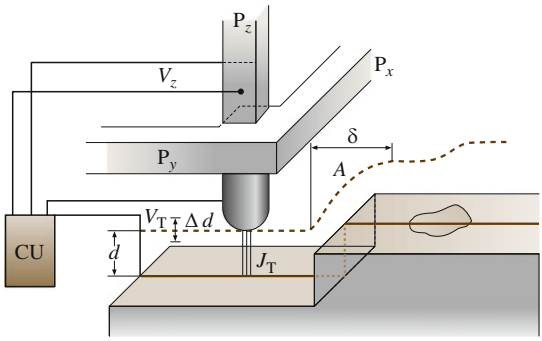

Fig. 2.2 Principle of operation of the STM, from Binnig and Rohrer [103]

2.1.1 The STM Design of Binnig et al.

Figure 2.2 shows a schematic of an AFM designed by Binnig and Rohrer and intended for operation in ultrahigh vacuum [1, 103]. The metal tip was fixed to rectangular piezodrives P_x, P_y, and P_z made out of commercial piezoceramic material for scanning. The sample is mounted via either superconducting magnetic levitation or a two-stage spring system to achieve a stable gap width of about 0.02 nm. The tunnel current J_T is a sensitive function of the gap width d where $J_T \propto V_T \exp(-A\phi^{1/2}d)$. Here V_T is the bias voltage, ϕ is the average barrier height (work function) and the constant $A = 1.025\ \mathrm{eV}^{-1/2}\ \mathrm{Å}^{-1}$. With a work function of a few eV, J_T changes by an order of magnitude for an angstrom change in d. If the current is kept constant to within, for example, 2%, then the gap d remains constant to within 1 pm. For operation in the constant current mode, the control unit CU applies a voltage V_z to the piezo P_z such that J_T remains constant when scanning the tip with P_y and P_x over the surface. At a constant work function ϕ, $V_z(V_x, V_y)$ yields the roughness of the surface $z(x, y)$ directly, as illustrated by a surface step at A. Smearing the step, δ (lateral resolution) is on the order of $(R)^{1/2}$, where R is the radius of the curvature of the tip. Thus, a lateral resolution of about 2 nm requires tip radii on the order of 10 nm. A 1 mm diameter solid rod ground at one end at roughly 90° yields overall tip radii of only a few hundred nanometers, the presence of rather sharp microtips on the relatively dull end yields a lateral resolution of about 2 nm. In situ sharpening of the tips, achieved by gently touching the surface, brings the resolution down to the 1 nm range; by applying high fields (on the order of 10^8 V/cm) for, say, half an hour, resolutions considerably below 1 nm can be reached. Most experiments have been performed with tungsten wires either ground or etched to a typical radius of 0.1–10 μm. In some cases, in situ processing of the tips has been performed to further reduce tip radii.

2.1.2 Commercial STMs

There are a number of commercial STMs available on the market. Digital Instruments, Inc., introduced the first commercial STM, the Nanoscope I, in 1987. In the

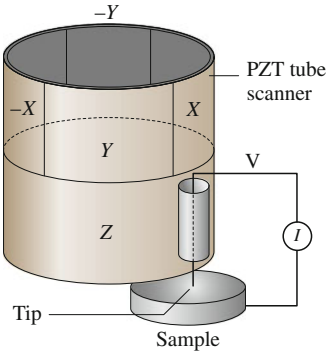

Fig. 2.3 Principle of operation of a commercial STM. A sharp tip attached to a piezoelectric tube scanner is scanned on a sample

recent Nanoscope IV STM, intended for operation in ambient air, the sample is held in position while a piezoelectric crystal in the form of a cylindrical tube (referred to as a PZT tube scanner) scans the sharp metallic probe over the surface in a raster pattern while sensing and relaying the tunneling current to the control station (Fig. 2.3). The digital signal processor (DSP) calculates the tip–sample separation required by sensing the tunneling current flowing between the sample and the tip. The bias voltage applied between the sample and the tip encourages the tunneling current to flow. The DSP completes the digital feedback loop by relaying the desired voltage to the piezoelectric tube. The STM can operate in either the *constant height* or the *constant current* mode, and this can be selected using the control panel. In the constant current mode, the feedback gains are set high, the tunneling tip closely tracks the sample surface, and the variation in the tip height required to maintain constant tunneling current is measured by the change in the voltage applied to the piezo tube. In the constant height mode, the feedback gains are set low, the tip remains at a nearly constant height as it sweeps over the sample surface, and the tunneling current is imaged.

Physically, the Nanoscope STM consists of three main parts: the head, which houses the piezoelectric tube scanner which provides three-dimensional tip motion and the preamplifier circuit for the tunneling current (FET input amplifier) mounted on the top of the head; the base on which the sample is mounted; and the base support, which supports the base and head [4]. The base accommodates samples which are up to 10 mm by 20 mm and 10 mm thick. Scan sizes available for the STM are 0.7 μm (for atomic resolution), 12 μm, 75 μm and 125 μm square.

The scanning head controls the three-dimensional motion of the tip. The removable head consists of a piezo tube scanner, about 12.7 mm in diameter, mounted into an Invar shell, which minimizes vertical thermal drift because of the good thermal match between the piezo tube and the Invar. The piezo tube has separate electrodes for *x*-, *y*- and *z*-motion, which are driven by separate drive circuits. The electrode configuration (Fig. 2.3) provides *x*- and *y*-motions which are perpendicular to each other, it minimizes horizontal and vertical coupling, and it provides good sensitivity. The vertical motion of the tube is controlled by the

Z-electrode, which is driven by the feedback loop. The *x*- and *y*-scanning motions are each controlled by two electrodes which are driven by voltages of the same magnitude but opposite signs. These electrodes are called $-y$, $-x$, $+y$, and $+x$. Applying complimentary voltages allows a short, stiff tube to provide a good scan range without the need for a large voltage. The motion of the tip that arises due to external vibrations is proportional to the square of the ratio of vibration frequency to the resonant frequency of the tube. Therefore, to minimize the tip vibrations, the resonant frequencies of the tube are high: about 60 kHz in the vertical direction and about 40 kHz in the horizontal direction. The tip holder is a stainless steel tube with an inner diameter of 300 μm when 250 μm diameter tips are used, which is mounted in ceramic in order to minimize the mass at the end of the tube. The tip is mounted either on the front edge of the tube (to keep the mounting mass low and the resonant frequency high) (Fig. 2.3) or the center of the tube for large-range scanners, namely 75 and 125 μm (to preserve the symmetry of the scanning). This commercial STM accepts any tip with a 250 μm diameter shaft. The piezotube requires *x*–*y*-calibration, which is carried out by imaging an appropriate calibration standard. Cleaved graphite is used for heads with small scan lengths while two-dimensional grids (a gold-plated rule) can be used for long-range heads.

The Invar base holds the sample in position, supports the head, and provides coarse *x*–*y*-motion for the sample. A sprung-steel sample clip with two thumb screws holds the sample in place. An *x*–*y*-translation stage built into the base allows the sample to be repositioned under the tip. Three precision screws arranged in a triangular pattern support the head and provide coarse and fine adjustment of the tip height. The base support consists of the base support ring and the motor housing. The stepper motor enclosed in the motor housing allows the tip to be engaged and withdrawn from the surface automatically.

Samples to be imaged with the STM must be conductive enough to allow a few nanoamperes of current to flow from the bias voltage source to the area to be scanned. In many cases, nonconductive samples can be coated with a thin layer of a conductive material to facilitate imaging. The bias voltage and the tunneling current depend on the sample. Usually they are set to a standard value for engagement and fine tuned to enhance the quality of the image. The scan size depends on the sample and the features of interest. A maximum scan rate of 122 Hz can be used. The maximum scan rate is usually related to the scan size. Scan rates above 10 Hz are used for small scans (typically 60 Hz for atomic-scale imaging with a 0.7 μm scanner). The scan rate should be lowered for large scans, especially if the sample surfaces are rough or contain large steps. Moving the tip quickly along the sample surface at high scan rates with large scan sizes will usually lead to a tip crash. Essentially, the scan rate should be inversely proportional to the scan size (typically 2–4 Hz for a scan size of 1 μm, 0.5–1 Hz for 12 μm, and 0.2 Hz for 125 μm). The scan rate (in length/time) is equal to the scan length divided by the scan rate in Hz. For example, for a scan size of 10 μm × 10 μm scanned at 0.5 Hz, the scan rate is 10 μm/s. 256 × 256 data formats are the most common. The lateral resolution at larger scans is approximately equal to scan length divided by 256.

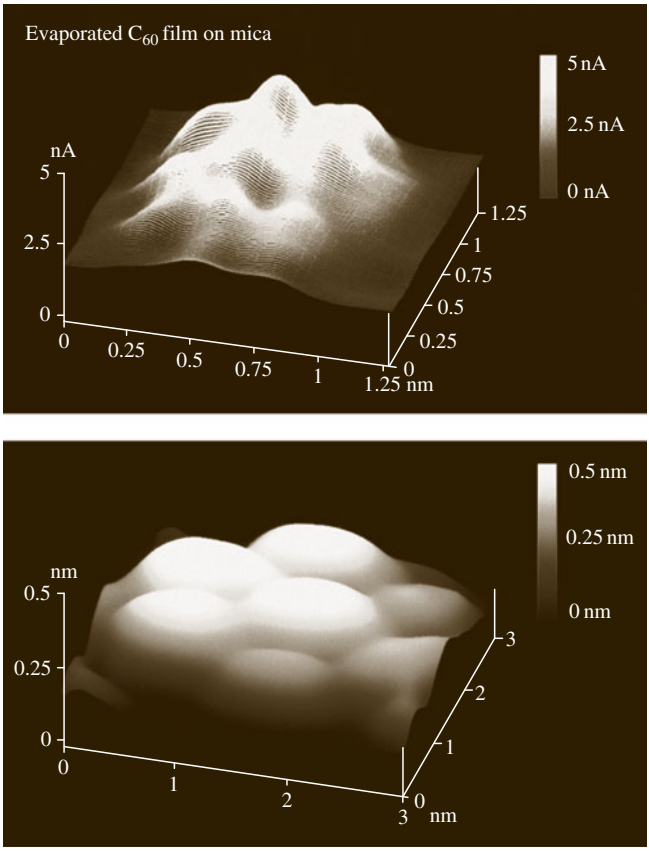

Fig. 2.4 STM images of evaporated C_{60} film on gold-coated freshly cleaved mica obtained using a mechanically sheared Pt-Ir (80/20) tip in constant height mode (After [104])

Figure 2.4 shows sample STM images of an evaporated C_{60} film on gold-coated freshly-cleaved mica taken at room temperature and ambient pressure [104]. Images were obtained with atomic resolution at two scan sizes. Next we describe some STM designs which are available for special applications.

Electrochemical STM

The electrochemical STM is used to perform and monitor the electrochemical reactions inside the STM. It includes a microscope base with an integral potentiostat, a short head with a 0.7 μm scan range and a differential preamp as well as the software required to operate the potentiostat and display the result of the electrochemical reaction.

Standalone STM

Standalone STMs are available to scan large samples. In this case, the STM rests directly on the sample. It is available from Digital Instruments in scan ranges of 12 and 75 μm. It is similar to the standard STM design except the sample base has been eliminated.

2.1.3 STM Probe Construction

The STM probe has a cantilever integrated with a sharp metal tip with a low aspect ratio (tip length/tip shank) to minimize flexural vibrations. Ideally, the tip should be atomically sharp, but in practice most tip preparation methods produce a tip with a rather ragged profile that consists of several asperities where the one closest to the surface is responsible for tunneling. STM cantilevers with sharp tips are typically fabricated from metal wires (the metal can be tungsten (W), platinum-iridium (Pt-Ir), or gold (Au)) and are sharpened by grinding, cutting with a wire cutter or razor blade, field emission/evaporation, ion milling, fracture, or electrochemical polishing/etching [105, 106]. The two most commonly used tips are made from either Pt-Ir (80/20) alloy or tungsten wire. Iridium is used to provide stiffness. The Pt-Ir tips are generally formed mechanically and are readily available. The tungsten tips are etched from tungsten wire by an electrochemical process, for example by using 1 M KOH solution with a platinum electrode in a electrochemical cell at about 30 V. In general, Pt-Ir tips provide better atomic resolution than tungsten tips, probably due to the lower reactivity of Pt. However, tungsten tips are more uniformly shaped and may perform better on samples with steeply sloped features. The tungsten wire diameter used for the cantilever is typically 250 μm, with the radius of curvature ranging from 20 to 100 nm and a cone angle ranging from 10° to 60° (Fig. 2.5). The wire can be bent in an L shape, if so required, for use in the instrument. For calculations of the normal spring constant and the natural frequency of round cantilevers, see Sarid and Elings [94].

High aspect ratio, controlled geometry (CG) Pt-Ir probes are commercially available to image deep trenches (Fig. 2.6). These probes are electrochemically etched from Pt-Ir (80/20) wire and are polished to a specific shape which is consistent from tip to tip. The probes have a full cone angle of ≈15°, and a tip radius of less than 50 nm. To image very deep trenches (>0.25 μm) and nanofeatures, focused ion beam (FIB)-milled CG probes with extremely sharp

Fig. 2.5 Schematic of a typical tungsten cantilever with a sharp tip produced by electrochemical etching

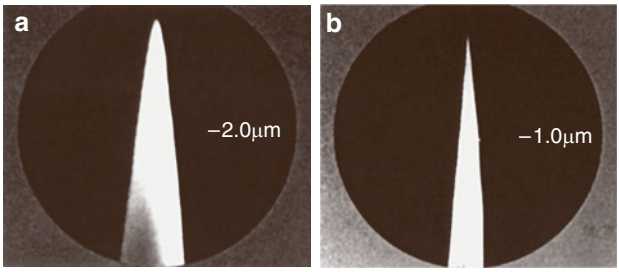

Fig. 2.6 Schematics of **(a)** CG Pt-Ir probe, and **(b)** CG Pt-Ir FIB milled probe

tips (radii <5 nm) are used. The Pt-Ir probes are coated with a nonconducting film (not shown in the figure) for electrochemistry. These probes are available from Materials Analytical Services (Raleigh, USA).

Pt alloy and W tips are very sharp and give high resolution, but are fragile and sometimes break when contacting a surface. Diamond tips have been used by Kaneko and Oguchi [107]. Diamond tips made conductive by boron ion implantation were found to be chip-resistant.

2.2 Atomic Force Microscope

Like the STM, the AFM relies on a scanning technique to produce very high resolution 3-D images of sample surfaces. The AFM measures ultrasmall forces (less than 1 nN) present between the AFM tip surface and a sample surface. These small forces are measured by measuring the motion of a very flexible cantilever beam with an ultrasmall mass. While STMs require the surface being measured be electrically conductive, AFMs are capable of investigating the surfaces of both conductors and insulators on an atomic scale if suitable techniques for measuring the cantilever motion are used. During the operation of a high-resolution AFM, the sample is generally scanned instead of the tip (unlike for STM) because the AFM measures the relative displacement between the cantilever surface and the reference surface and any cantilever movement from scanning would add unwanted vibrations. However, for measurements of large samples, AFMs are available where the tip is scanned and the sample is stationary. As long as the AFM is operated in the so-called contact mode, little if any vibration is introduced.

The AFM combines the principles of the STM and the stylus profiler (Fig. 2.7). In an AFM, the force between the sample and tip is used (rather than the tunneling current) to sense the proximity of the tip to the sample. The AFM can be used either in the static or the dynamic mode. In the static mode, also referred to as the repulsive or contact mode [2], a sharp tip at the end of the cantilever is brought into contact with the surface of the sample. During initial contact, the atoms at the

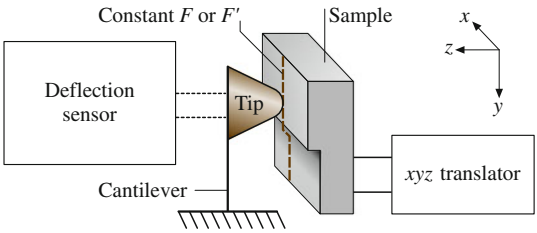

Fig. 2.7 Principle of operation of the AFM. Sample mounted on a piezoelectric scanner is scanned against a short tip and the cantilever deflection is usually measured using a laser deflection technique. The force (in contact mode) or the force gradient (in noncontact mode) is measured during scanning

end of the tip experience a very weak repulsive force due to electronic orbital overlap with the atoms in the surface of the sample. The force acting on the tip causes the cantilever to deflect, which is measured by tunneling, capacitive, or optical detectors. The deflection can be measured to within 0.02 nm, so a force as low as 0.2 nN (corresponding to a normal pressure of ≈200 MPa for a Si_3N_4 tip with a radius of about 50 nm against single-crystal silicon) can be detected for typical cantilever spring constant of 10 N/m. (To put these number in perspective, individual atoms and human hair are typically a fraction of a nanometer and about 75 μm in diameter, respectively, and a drop of water and an eyelash have masses of about 10 μN and 100 nN, respectively.) In the dynamic mode of operation, also referred to as attractive force imaging or noncontact imaging mode, the tip is brought into close proximity to (within a few nanometers of), but not in contact with, the sample. The cantilever is deliberately vibrated in either amplitude modulation (AM) mode [65] or frequency modulation (FM) mode [65, 94, 108, 109]. Very weak van der Waals attractive forces are present at the tip–sample interface. Although the normal pressure exerted at the interface is zero in this technique (in order to avoid any surface deformation), it is slow and difficult to use, and is rarely used outside of research environments. The surface topography is measured by laterally scanning the sample under the tip while simultaneously measuring the separation-dependent force or force gradient (derivative) between the tip and the surface (Fig. 2.7). In the contact (static) mode, the interaction force between tip and sample is measured by monitoring the cantilever deflection. In the noncontact (or dynamic) mode, the force gradient is obtained by vibrating the cantilever and measuring the shift in the resonant frequency of the cantilever. To obtain topographic information, the interaction force is either recorded directly, or used as a control parameter for a feedback circuit that maintains the force or force derivative at a constant value. Using an AFM operated in the contact mode, topographic images with a vertical resolution of less than 0.1 nm (as low as 0.01 nm) and a lateral resolution of about 0.2 nm have been obtained [3, 50, 110, 111, 112, 113, 114]. Forces of 10 nN to 1 pN are measurable with a displacement sensitivity of 0.01 nm. These forces are comparable to the forces associated with chemical bonding, for example 0.1 μN for an ionic

bond and 10 pN for a hydrogen bond [2]. For further reading, see [94, 95, 96, 100, 102, 115, 116, 117, 118, 119].

Lateral forces applied at the tip during scanning in the contact mode affect roughness measurements [120]. To minimize the effects of friction and other lateral forces on topography measurements in the contact mode, and to measure the topographies of soft surfaces, AFMs can be operated in the so-called tapping or force modulation mode [32, 121].

The STM is ideal for atomic-scale imaging. To obtain atomic resolution with the AFM, the spring constant of the cantilever should be weaker than the equivalent spring between atoms. For example, the vibration frequencies ω of atoms bound in a molecule or in a crystalline solid are typically 10^{13} Hz or higher. Combining this with an atomic mass m of $\approx 10^{25}$ kg gives an interatomic spring constant k, given by $\omega^2 m$, of around 10 N/m [115]. (For comparison, the spring constant of a piece of household aluminium foil that is 4 mm long and 1 mm wide is about 1 N/m.) Therefore, a cantilever beam with a spring constant of about 1 N/m or lower is desirable. Tips must be as sharp as possible, and tip radii of 5–50 nm are commonly available.

Atomic resolution cannot be achieved with these tips at normal loads in the nN range. Atomic structures at these loads have been obtained from lattice imaging or by imaging the crystal's periodicity. Reported data show either perfectly ordered periodic atomic structures or defects on a larger lateral scale, but no well-defined, laterally resolved atomic-scale defects like those seen in images routinely obtained with a STM. Interatomic forces with one or several atoms in contact are 20–40 or 50–100 pN, respectively. Thus, atomic resolution with an AFM is only possible with a sharp tip on a flexible cantilever at a net repulsive force of 100 pN or lower [122]. Upon increasing the force from 10 pN, Ohnesorge and Binnig [122] observed that monoatomic steplines were slowly wiped away and a perfectly ordered structure was left. This observation explains why mostly defect-free atomic resolution has been observed with AFM. Note that for atomic-resolution measurements, the cantilever should not be so soft as to avoid jumps. Further note that performing measurements in the noncontact imaging mode may be desirable for imaging with atomic resolution.

The key component in an AFM is the sensor used to measure the force on the tip due to its interaction with the sample. A cantilever (with a sharp tip) with an extremely low spring constant is required for high vertical and lateral resolutions at small forces (0.1 nN or lower), but a high resonant frequency is desirable (about 10–100 kHz) at the same time in order to minimize the sensitivity to building vibrations, which occur at around 100 Hz. This requires a spring with an extremely low vertical spring constant (typically 0.05–1 N/m) as well as a low mass (on the order of 1 ng). Today, the most advanced AFM cantilevers are microfabricated from silicon or silicon nitride using photolithographic techniques. Typical lateral dimensions are on the order of 100 μm, with thicknesses on the order of 1 μm. The force on the tip due to its interaction with the sample is sensed by detecting the deflection of the compliant lever with a known spring constant. This cantilever deflection (displacement smaller than 0.1 nm) has been measured by detecting a

tunneling current similar to that used in the STM in the pioneering work of Binnig et al. [2] and later used by Giessibl et al. [56], by capacitance detection [123, 124], piezoresistive detection [125, 126], and by four optical techniques, namely (1) optical interferometry [5, 6, 127, 128] using optical fibers [57, 129] (2) optical polarization detection [72, 130], (3) laser diode feedback [131] and (4) optical (laser) beam deflection [7, 8, 53, 111, 112]. Schematics of the four more commonly used detection systems are shown in Fig. 2.8. The tunneling method originally used by Binnig et al. [2] in the first version of the AFM uses a second tip to monitor the deflection of the cantilever with its force sensing tip. Tunneling is rather sensitive to contaminants and the interaction between the tunneling tip and the rear side of the cantilever can become comparable to the interaction between the tip and sample. Tunneling is rarely used and is mentioned mainly for historical reasons. Giessibl et al. [56] have used it for a low-temperature AFM/STM design. In contrast to tunneling, other deflection sensors are placed far from the cantilever, at distances of micrometers to tens of millimeters. The optical techniques are believed to be more sensitive, reliable and easily implemented detection methods than the others [94, 118]. The optical beam deflection method has the largest working distance, is insensitive to distance changes and is capable of measuring angular changes (friction forces); therefore, it is the most commonly used in commercial SPMs.

Almost all SPMs use piezo translators to scan the sample, or alternatively to scan the tip. An electric field applied across a piezoelectric material causes a change in the crystal structure, with expansion in some directions and contraction in others. A net change in volume also occurs [132]. The first STM used a piezo tripod for scanning [1]. The piezo tripod is one way to generate three-dimensional movement of a tip attached at its center. However, the tripod needs to be fairly large (≈50 mm) to get a suitable range. Its size and asymmetric shape makes it susceptible to thermal drift. Tube scanners are widely used in AFMs [133]. These provide ample scanning range with a small size. Electronic control systems for AFMs are

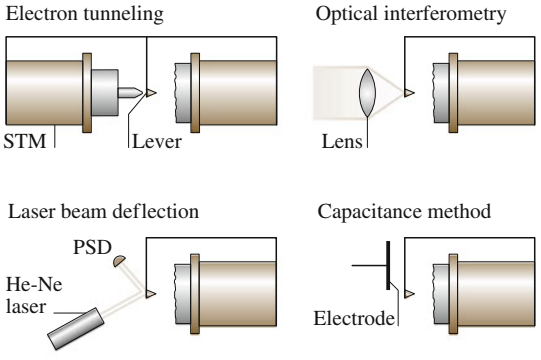

Fig. 2.8 Schematics of the four detection systems to measure cantilever deflection. In each set-up, the sample mounted on piezoelectric body is shown *on the right*, the cantilever *in the middle*, and the corresponding deflection sensor *on the left* (After [118])

based on either analog or digital feedback. Digital feedback circuits are better suited for ultralow noise operation.

Images from the AFMs need to be processed. An ideal AFM is a noise-free device that images a sample with perfect tips of known shape and has a perfectly linear scanning piezo. In reality, scanning devices are affected by distortions and these distortions must be corrected for. The distortions can be linear and nonlinear. Linear distortions mainly result from imperfections in the machining of the piezo translators, causing cross-talk between the *Z*-piezo to the *x*- and *y*-piezos, and vice versa. Nonlinear distortions mainly result from the presence of a hysteresis loop in piezoelectric ceramics. They may also occur if the scan frequency approaches the upper frequency limit of the *x*- and *y*-drive amplifiers or the upper frequency limit of the feedback loop (*z*-component). In addition, electronic noise may be present in the system. The noise is removed by digital filtering in real space [134] or in the spatial frequency domain (Fourier space) [135].

Processed data consists of many tens of thousand of points per plane (or data set). The outputs from the first STM and AFM images were recorded on an *x*–*y*-chart recorder, with the *z*-value plotted against the tip position in the fast scan direction. Chart recorders have slow responses, so computers are used to display the data these days. The data are displayed as wire mesh displays or grayscale displays (with at least 64 shades of gray).

2.2.1 The AFM Design of Binnig et al.

In the first AFM design developed by Binnig et al. [2], AFM images were obtained by measuring the force exerted on a sharp tip created by its proximity to the surface of a sample mounted on a 3-D piezoelectric scanner. The tunneling current between the STM tip and the backside of the cantilever beam to which the tip was attached was measured to obtain the normal force. This force was kept at a constant level with a feedback mechanism. The STM tip was also mounted on a piezoelectric element to maintain the tunneling current at a constant level.

2.2.2 Commercial AFMs

A review of early designs of AFMs has been presented by Bhushan [4]. There are a number of commercial AFMs available on the market. Major manufacturers of AFMs for use in ambient environments are: Digital Instruments, Inc., Topometrix Corp. and other subsidiaries of Veeco Instruments, Inc., Molecular Imaging Corp. (Phoenix, USA), Quesant Instrument Corp. (Agoura Hills, USA), Nanoscience Instruments, Inc. (Phoenix, USA), Seiko Instruments (Chiba, Japan); and Olympus

(Tokyo, Japan). AFM/STMs for use in UHV environments are manufactured by Omicron Vakuumphysik GmbH (Taunusstein, Germany).

We describe here two commercial AFMs – small-sample and large-sample AFMs – for operation in the contact mode, produced by Digital Instruments, Inc., with scanning lengths ranging from about 0.7 μm (for atomic resolution) to about 125 μm [9, 111, 114, 136]. The original design of these AFMs comes from Meyer and Amer [53]. Basically, the AFM scans the sample in a raster pattern while outputting the cantilever deflection error signal to the control station. The cantilever deflection (or the force) is measured using a laser deflection technique (Fig. 2.9). The DSP in the workstation controls the z-position of the piezo based on the cantilever deflection error signal. The AFM operates in both *constant height* and *constant force* modes. The DSP always adjusts the distance between the sample and the tip according to the cantilever deflection error signal, but if the feedback gains are low the piezo remains at an almost *constant height* and the cantilever deflection data is collected. With high gains, the piezo height changes to keep the cantilever deflection nearly constant (so the force is constant), and the change in piezo height is collected by the system.

In the operation of a commercial small-sample AFM (as shown in Fig. 2.9a), the sample (which is generally no larger than 10 mm $\times$ 10 mm) is mounted on a PZT tube scanner, which consists of separate electrodes used to precisely scan the sample in the x–y-plane in a raster pattern and to move the sample in the vertical (z-) direction. A sharp tip at the free end of a flexible cantilever is brought into contact with the sample. Features on the sample surface cause the cantilever to deflect in the vertical and lateral directions as the sample moves under the tip. A laser beam from a diode laser (5 mW max. peak output at 670 nm) is directed by a prism onto the back of a cantilever near its free end, tilted downward at about 10° with respect to the horizontal plane. The reflected beam from the vertex of the cantilever is directed through a mirror onto a quad photodetector (split photodetector with four quadrants) (commonly called a position-sensitive detector or PSD, produced by Silicon Detector Corp., Camarillo, USA). The difference in signal between the top and bottom photodiodes provides the AFM signal, which is a sensitive measure of the cantilever vertical deflection. The topographic features of the sample cause the tip to deflect in the vertical direction as the sample is scanned under the tip. This tip deflection will change the direction of the reflected laser beam, changing the intensity difference between the top and bottom sets of photodetectors (AFM signal). In a mode of operation called the height mode, used for topographic imaging or for any other operation in which the normal forceapplied is to be kept constant, a feedback circuit is used to modulate the voltage applied to the PZT scanner in order to adjust the height of the PZT, so that the cantilever vertical deflection (given by the intensity difference between the top and bottom detector) will remain constant during scanning. The PZT height variation is thus a direct measure of the surface roughness of the sample.

In a large-sample AFM, force sensors based on optical deflection methods or scanning units are mounted on the microscope head (Fig. 2.9b). Because of the

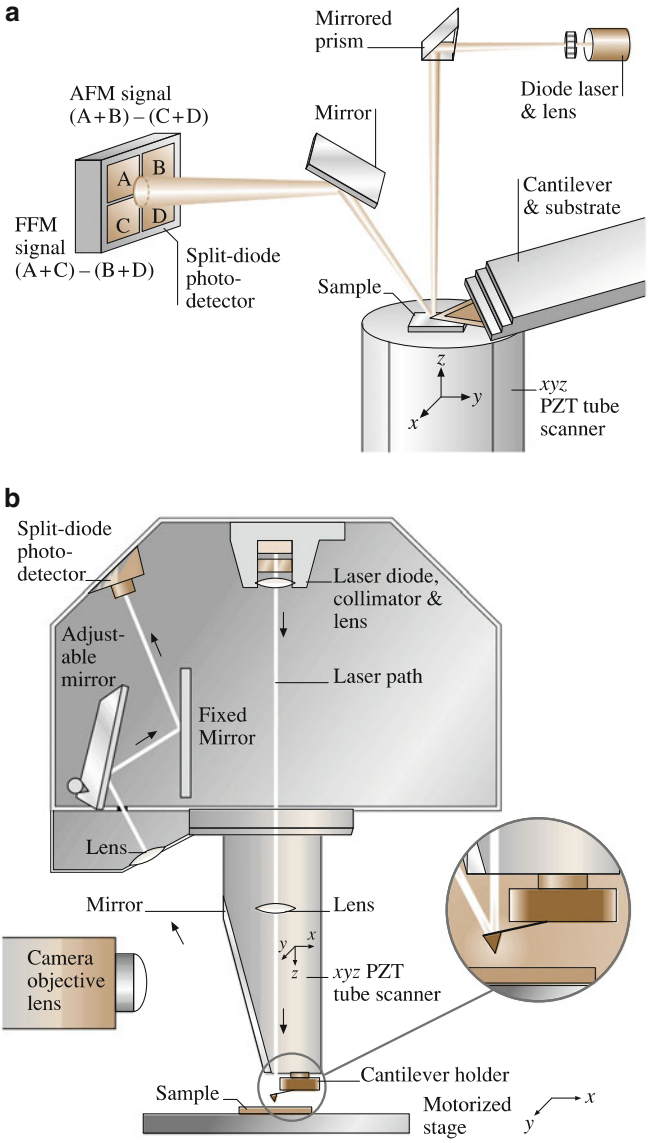

Fig. 2.9 Principles of operation of (**a**) a commercial small-sample AFM/FFM, and (**b**) a large-sample AFM/FFM

unwanted vibrations caused by cantilever movement, the lateral resolution of this design is somewhat poorer than the design in Fig. 2.9a in which the sample is scanned instead of the cantilever beam. The advantage of the large-sample AFM is that large samples can be easily measured.

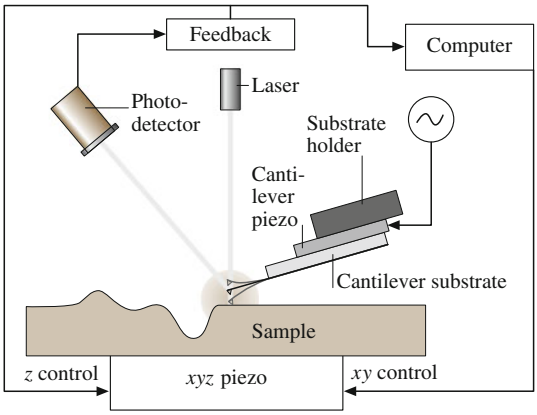

Fig. 2.10 Schematic of tapping mode used for surface roughness measurements

Most AFMs can be used for topography measurements in the so-called tapping mode (intermittent contact mode), in what is also referred to as dynamic force microscopy. In the tapping mode, during the surface scan, the cantilever/tip assembly is sinusoidally vibrated by a piezo mounted above it, and the oscillating tip slightly taps the surface at the resonant frequency of the cantilever (70–400 kHz) with a constant (20–100 nm) amplitude of vertical oscillation, and a feedback loop keeps the average normal force constant (Fig. 2.10). The oscillating amplitude is kept large enough that the tip does not get stuck to the sample due to adhesive attraction. The tapping mode is used in topography measurements to minimize the effects of friction and other lateral forces to measure the topography of soft surfaces.

Topographic measurements can be made at any scanning angle. At first glance, the scanning angle may not appear to be an important parameter. However, the friction force between the tip and the sample will affect the topographic measurements in a parallel scan (scanning along the long axis of the cantilever). This means that a perpendicular scan may be more desirable. Generally, one picks a scanning angle which gives the same topographic data in both directions; this angle may be slightly different to that for the perpendicular scan.

The left-hand and right-hand quadrants of the photodetector are used to measure the friction force applied at the tip surface during sliding. In the so-called friction mode, the sample is scanned back and forth in a direction orthogonal to the long axis of the cantilever beam. Friction force between the sample and the tip will twist the cantilever. As a result, the laser beam will be deflected out of the plane defined by the incident beam and the beam is reflected vertically from an untwisted cantilever. This produces a difference in laser beam intensity between the beams received by the left-hand and right-hand sets of quadrants of the photodetector. The intensity difference between the two sets of detectors (FFM signal) is directly related to the degree of twisting and hence to the magnitude of the friction force. This method provides three-dimensional maps of the friction force. One problem

associated with this method is that any misalignment between the laser beam and the photodetector axis introduces errors into the measurement. However, by following the procedures developed by Ruan and Bhushan [136], in which the average FFM signal for the sample scanned in two opposite directions is subtracted from the friction profiles of each of the two scans, the misalignment effect can be eliminated. By following the friction force calibration procedures developed by Ruan and Bhushan [136], voltages corresponding to friction forces can be converted to force units. The coefficient of friction is obtained from the slope of the friction force data measured as a function of the normal load, which typically ranges from 10 to 150 nN. This approach eliminates any contributions from adhesive forces [10]. To calculate the coefficient of friction based on a single point measurement, the friction force should be divided by the sum of the normal load applied and the intrinsic adhesive force. Furthermore, it should be pointed out that the coefficient of friction is not independent of load for single-asperity contact. This is discussed in more detail later.

The tip is scanned in such a way that its trajectory on the sample forms a triangular pattern (Fig. 2.11). Scanning speeds in the fast and slow scan directions depend on the scan area and scan frequency. Scan sizes ranging from less than 1 nm × 1 nm to 125 μm × 125 μm and scan rates of less than 0.5–122 Hz are typically used. Higher scan rates are used for smaller scan lengths. For example, the scan rates in the fast and slow scan directions for an area of 10 μm × 10 μm scanned at 0.5 Hz are 10 μm/s and 20 nm/s, respectively.

We now describe the construction of a small-sample AFM in more detail. It consists of three main parts: the optical head which senses the cantilever deflection; a PZT tube scanner which controls the scanning motion of the sample mounted on one of its ends; and the base, which supports the scanner and head and includes circuits for the deflection signal (Fig. 2.12a). The AFM connects directly to a control system. The optical head consists of a laser diode stage, a photodiode stage preamp board, the cantilever mount and its holding arm, and the deflected beam reflecting mirror, which reflects the deflected beam toward the photodiode (Fig. 2.12b). The laser diode stage is a tilt stage used to adjust the position of the laser beam relative to the cantilever. It consists of the laser diode, collimator, focusing lens, baseplate, and the *x*- and *y*-laser diode positioners. The positioners are used to place the laser spot on the end of the cantilever. The photodiode stage is an adjustable stage used to position the photodiode elements relative to the reflected

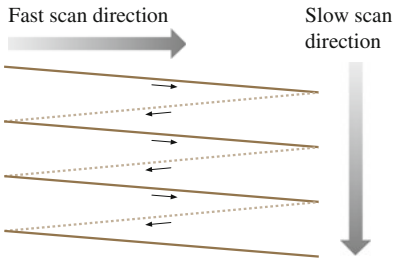

Fig. 2.11 Schematic of triangular pattern trajectory of the AFM tip as the sample is scanned in two dimensions. During imaging, data are only recorded during scans along the *solid scan lines*

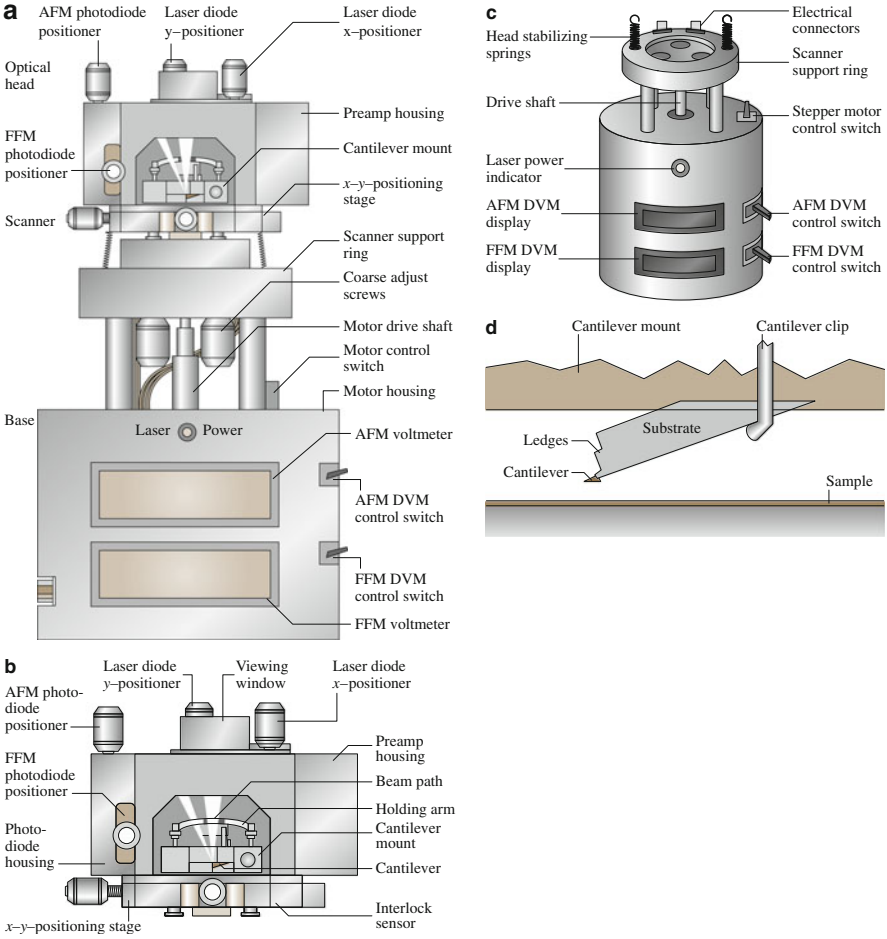

Fig. 2.12 Schematics of a commercial AFM/FFM made by Digital Instruments, Inc. **(a)** Front view, **(b)** optical head, **(c)** base, and **(d)** cantilever substrate mounted on cantilever mount (not to scale)

laser beam. It consists of the split photodiode, the base plate, and the photodiode positioners. The deflected beam reflecting mirror is mounted on the upper left in the interior of the head. The cantilever mount is a metal (for operation in air) or glass (for operation in water) block which holds the cantilever firmly at the proper angle (Fig. 2.12d). Next, the tube scanner consists of an Invar cylinder holding a single tube made of piezoelectric crystal which imparts the necessary three-dimensional motion to the sample. Mounted on top of the tube is a magnetic cap on which the steel sample puck is placed. The tube is rigidly held at one end with the sample mounted on the other end of the tube. The scanner also contains three fine-pitched screws which form the mount for the optical head. The optical head rests on the tips

of the screws, which are used to adjust the position of the head relative to the sample. The scanner fits into the scanner support ring mounted on the base of the microscope (Fig. 2.12c). The stepper motor is controlled manually with the switch on the upper surface of the base and automatically by the computer during the tip–engage and tip–withdraw processes.

The scan sizes available for these instruments are 0.7, 12 and 125 μm. The scan rate must be decreased as the scan size is increased. A maximum scan rate of 122 Hz can be used. Scan rates of about 60 Hz should be used for small scan lengths (0.7 μm). Scan rates of 0.5–2.5 Hz should be used for large scans on samples with tall features. High scan rates help reduce drift, but they can only be used on flat samples with small scan sizes. The scan rate or the scanning speed (length/time) in the fast scan direction is equal to twice the scan length multiplied by the scan rate in Hz, and in the slow direction it is equal to the scan length multiplied by the scan rate in Hz divided by number of data points in the transverse direction. For example, for a scan size of 10 μm × 10 μm scanned at 0.5 Hz, the scan rates in the fast and slow scan directions are 10 μm/s and 20 nm/s, respectively. Normally 256 × 256 data points are taken for each image. The lateral resolution at larger scans is approximately equal to the scan length divided by 256. The piezo tube requires *x*–*y*-calibration, which is carried out by imaging an appropriate calibration standard. Cleaved graphite is used for small scan heads, while two-dimensional grids (a gold-plated rule) can be used for long-range heads.

Examples of AFM images of freshly cleaved highly oriented pyrolytic (HOP) graphite and mica surfaces are shown in Fig. 2.13 [50, 110, 114]. Images with near-atomic resolution are obtained.

The force calibration mode is used to study interactions between the cantilever and the sample surface. In the force calibration mode, the *x*- and *y*-voltages applied to the piezo tube are held at zero and a sawtooth voltage is applied to the *z*-electrode of the piezo tube (Fig. 2.14a). At the start of the force measurement the cantilever is in its rest position. By changing the applied voltage, the sample can be moved up and down relative to the stationary cantilever tip. As the piezo moves the sample up and down, the cantilever deflection signal from the photodiode is monitored. The force–distance curve, a plot of the cantilever tip deflection signal as a function of the voltage applied to the piezo tube, is obtained. Figure 2.14b shows the typical features of a force–distance curve. The arrowheads indicate the direction of piezo travel. As the piezo extends, it approaches the tip, which is in mid-air at this point and hence shows no deflection. This is indicated by the flat portion of the curve. As the tip approaches the sample to within a few nanometers (point A), an attractive force kicks in between the atoms of the tip surface and the atoms of the surface of the sample. The tip is pulled towards the sample and contact occurs at point B on the graph. From this point on, the tip is in contact with the surface, and as the piezo extends further, the tip gets deflected further. This is represented by the sloped portion of the curve. As the piezo retracts, the tip moves beyond the zero deflection (flat) line due to attractive forces (van der Waals forces and long-range meniscus forces), into the adhesive regime. At point C in the graph, the tip snaps free of the

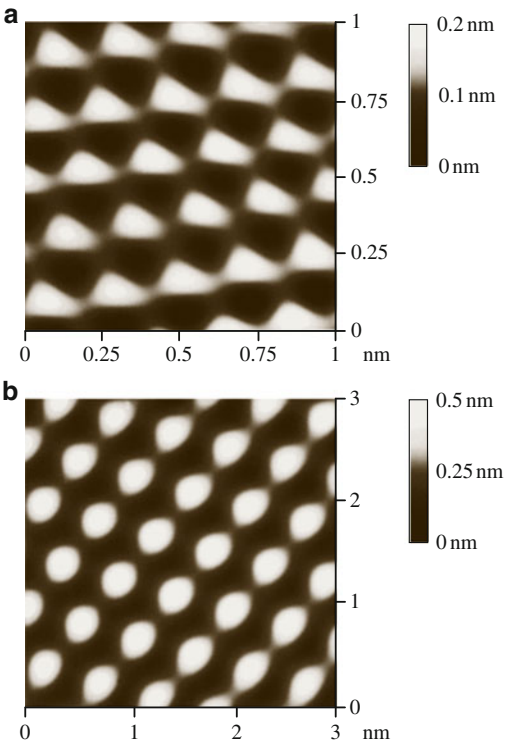

Fig. 2.13 Typical AFM images of freshly-cleaved **(a)** highly oriented pyrolytic graphite and **(b)** mica surfaces taken using a square pyramidal Si_3N_4 tip

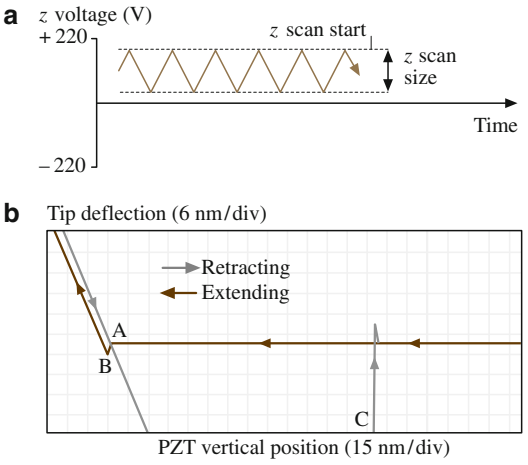

Fig. 2.14 **(a)** Force calibration Z waveform, and **(b)** a typical force–distance curve for a tip in contact with a sample. Contact occurs at point B; tip breaks free of adhesive forces at point C as the sample moves away from the tip

adhesive forces, and is again in free air. The horizontal distance between points B and C along the retrace line gives the distance moved by the tip in the adhesive regime. Multiplying this distance by the stiffness of the cantilever gives the

adhesive force. Incidentally, the horizontal shift between the loading and unloading curves results from the hysteresis in the PZT tube [4].

Multimode Capabilities

The multimode AFM can be used for topography measurements in the contact mode and tapping mode, described earlier, and for measurements of lateral (friction) force, electric force gradients and magnetic force gradients.

The multimode AFM, when used with a grounded conducting tip, can be used to measure electric field gradients by oscillating the tip near its resonant frequency. When the lever encounters a force gradient from the electric field, the effective spring constant of the cantilever is altered, changing its resonant frequency. Depending on which side of the resonance curve is chosen, the oscillation amplitude of the cantilever increases or decreases due to the shift in the resonant frequency. By recording the amplitude of the cantilever, an image revealing the strength of the electric field gradient is obtained.

In the magnetic force microscope (MFM), used with a magnetically coated tip, static cantilever deflection is detected when a magnetic field exerts a force on the tip, and MFM images of magnetic materials can be obtained. MFM sensitivity can be enhanced by oscillating the cantilever near its resonant frequency. When the tip encounters a magnetic force gradient, the effective spring constant (and hence the resonant frequency) is shifted. By driving the cantilever above or below the resonant frequency, the oscillation amplitude varies as the resonance shifts. An image of the magnetic field gradient is obtained by recording the oscillation amplitude as the tip is scanned over the sample.

Topographic information is separated from the electric field gradient and magnetic field images using the so-called lift mode. In lift mode, measurements are taken in two passes over each scan line. In the first pass, topographical information is recorded in the standard tapping mode, where the oscillating cantilever lightly taps the surface. In the second pass, the tip is lifted to a user-selected separation (typically 20–200 nm) between the tip and local surface topography. By using stored topographical data instead of standard feedback, the tip–sample separation can be kept constant. In this way, the cantilever amplitude can be used to measure electric field force gradients or relatively weak but long-range magnetic forces without being influenced by topographic features. Two passes are made for every scan line, producing separate topographic and magnetic force images.

Electrochemical AFM

This option allows one to perform electrochemical reactions on the AFM. The technique involves a potentiostat, a fluid cell with a transparent cantilever holder

and electrodes, and the software required to operate the potentiostat and display the results of the electrochemical reaction.

2.2.3 AFM Probe Construction

Various probes (cantilevers and tips) are used for AFM studies. The cantilever stylus used in the AFM should meet the following criteria: (1) low normal spring constant (stiffness); (2) high resonant frequency; (3) high cantilever quality factor Q; (4) high lateral spring constant (stiffness); (5) short cantilever length; (6) incorporation of components (such as mirror) for deflection sensing; and (7) a sharp protruding tip [137]. In order to register a measurable deflection with small forces, the cantilever must flex with a relatively low force (on the order of few nN), requiring vertical spring constants of 10^2–10^2 N/m for atomic resolution in the contact profiling mode. The data rate or imaging rate in the AFM is limited by the mechanical resonant frequency of the cantilever. To achieve a large imaging bandwidth, the AFM cantilever should have a resonant frequency of more than about 10 kHz (30–100 kHz is preferable), which makes the cantilever the least sensitive part of the system. Fast imaging rates are not just a matter of convenience, since the effects of thermal drifts are more pronounced with slow scanning speeds. The combined requirements of a low spring constant and a high resonant frequency are met by reducing the mass of the cantilever. The quality factor Q ($= \omega_R/(c/m)$, where ω_R is the resonant frequency of the damped oscillator, c is the damping constant and m is the mass of the oscillator) should have a high value for some applications. For example, resonance curve detection is a sensitive modulation technique for measuring small force gradients in noncontact imaging. Increasing the Q increases the sensitivity of the measurements. Mechanical Q values of 100–1,000 are typical. In contact modes, the Q value is of less importance. A high lateral cantilever spring constant is desirable in order to reduce the effect of lateral forces in the AFM, as frictional forces can cause appreciable lateral bending of the cantilever. Lateral bending results in erroneous topography measurements. For friction measurements, cantilevers with reduced lateral rigidity are preferred. A sharp protruding tip must be present at the end of the cantilever to provide a well-defined interaction with the sample over a small area. The tip radius should be much smaller than the radii of the corrugations in the sample in order for these to be measured accurately. The lateral spring constant depends critically on the tip length. Additionally, the tip should be centered at the free end.

In the past, cantilevers have been cut by hand from thin metal foils or formed from fine wires. Tips for these cantilevers were prepared by attaching diamond fragments to the ends of the cantilevers by hand, or in the case of wire cantilevers, electrochemically etching the wire to a sharp point. Several cantilever geometries for wire cantilevers have been used. The simplest geometry is the L-shaped cantilever, which is usually made by bending a wire at a 90° angle. Other geometries include single-V and double-V geometries, with a sharp tip attached at the

apex of the V, and double-X configuration with a sharp tip attached at the intersection [31, 138]. These cantilevers can be constructed with high vertical spring constants. For example, a double-cross cantilever with an effective spring constant of 250 N/m was used by Burnham and Colton [31]. The small size and low mass needed in the AFM make hand fabrication of the cantilever a difficult process with poor reproducibility. Conventional microfabrication techniques are ideal for constructing planar thin-film structures which have submicron lateral dimensions. The triangular (V-shaped) cantilevers have improved (higher) lateral spring constants in comparison to rectangular cantilevers. In terms of spring constants, the triangular cantilevers are approximately equivalent to two rectangular cantilevers placed in parallel [137]. Although the macroscopic radius of a photolithographically patterned corner is seldom much less than about 50 nm, microscopic asperities on the etched surface provide tips with near-atomic dimensions.

Cantilevers have been used from a whole range of materials. Cantilevers made of Si_3N_4, Si, and diamond are the most common. The Young's modulus and the density are the material parameters that determine the resonant frequency, aside from the geometry. Table 2.2 shows the relevant properties and the speed of sound, indicative of the resonant frequency for a given shape. Hardness is an important indicator of the durability of the cantilever, and is also listed in the table. Materials used for STM cantilevers are also included.

Silicon nitride cantilevers are less expensive than those made of other materials. They are very rugged and well suited to imaging in almost all environments. They are especially compatible with organic and biological materials. Microfabricated triangular silicon nitride beams with integrated square pyramidal tips made using plasma-enhanced chemical vapor deposition (PECVD) are the most common [137]. Four cantilevers, marketed by Digital Instruments, with different sizes and spring constants located on cantilever substrate made of boron silicate glass (Pyrex), are shown in Figs. 2.15a and 2.16. The two pairs of cantilevers on each substrate measure about 115 and 193 μm from the substrate to the apex of the triangular cantilever, with base widths of 122 and 205 μm, respectively. The cantilever legs, which are of the same thickness (0.6 μm) in all the cantilevers, are available in wide and narrow forms. Only one cantilever is selected and used from each substrate. The calculated spring constants and measured natural frequencies for each of the configurations are listed in Table 2.3. The most commonly used cantilever beam is the 115 μm long, wide-legged cantilever (vertical spring

Table 2.2 Relevant properties of materials used for cantilevers

Property	Young's modulus (E) (GPa)	Density (ρg) (kg/m^3)	Microhardness (GPa)	Speed of sound ($\sqrt{E/\rho}$) (m/s)
Diamond	900–1,050	3,515	78.4–102	17,000
Si_3N_4	310	3,180	19.6	9,900
Si	130–188	2,330	9–10	8,200
W	350	19,310	3.2	4,250
Ir	530	–	≈3	5,300

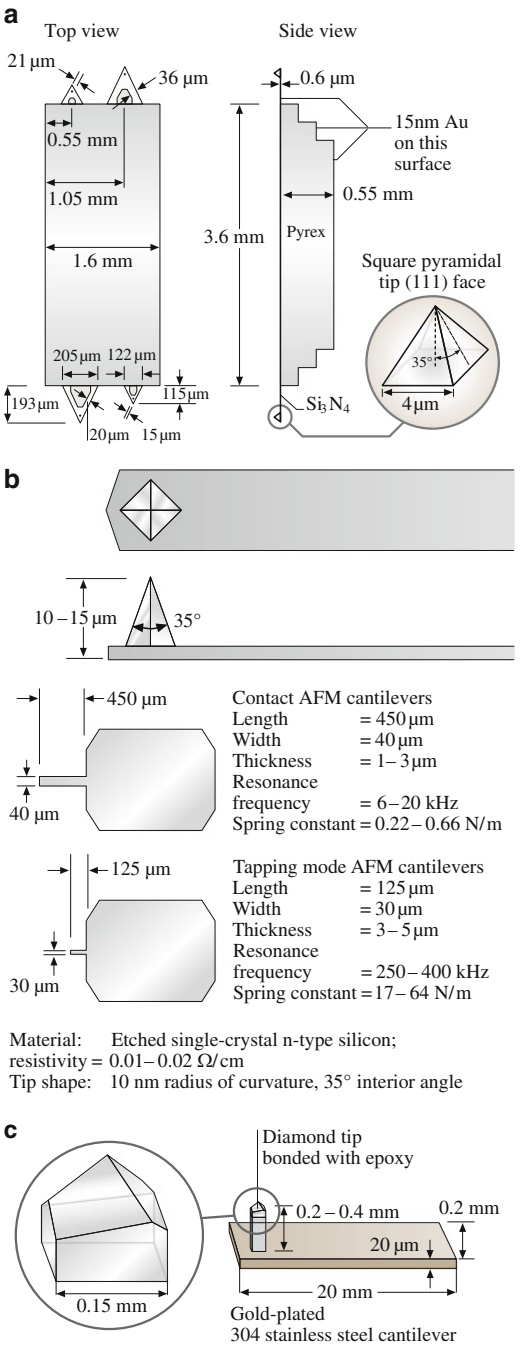

Fig. 2.15 Schematics of **(a)** triangular cantilever beam with square-pyramidal tips made of PECVD Si_3N_4, **(b)** rectangular cantilever beams with square-pyramidal tips made of etched single-crystal silicon, and **(c)** rectangular cantilever stainless steel beam with three-sided pyramidal natural diamond tip

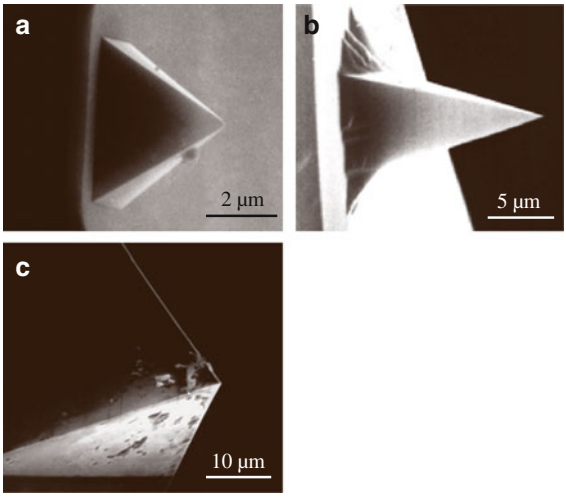

Fig. 2.16 SEM micrographs of a square-pyramidal PECVD Si_3N_4 tip **(a)**, a square-pyramidal etched single-crystal silicon tip **(b)**, and a three-sided pyramidal natural diamond tip **(c)**

Table 2.3 Measured vertical spring constants and natural frequencies of triangular (V-shaped) cantilevers made of PECVD Si_3N_4 (data provided by Digital Instruments, Inc.)

Cantilever dimension	Spring constant (k_z) (N/m)	Natural frequency (ω_0) (kHz)
115 μm long, narrow leg	0.38	40
115 μm long, wide leg	0.58	40
193 μm long, narrow leg	0.06	13–22
193 μm long, wide leg	0.12	13–22

constant = 0.58 N/m). Cantilevers with smaller spring constants should be used on softer samples. The pyramidal tip is highly symmetric, and the end has a radius of about 20–50 nm. The side walls of the tip have a slope of 35° and the lengths of the edges of the tip at the cantilever base are about 4 μm.

An alternative to silicon nitride cantilevers with integrated tips are microfabricated single-crystal silicon cantilevers with integrated tips. Si tips are sharper than Si_3N_4 tips because they are formed directly by anisotropic etching of single-crystal Si, rather than through the use of an etch pit as a mask for the deposited material [139]. Etched single-crystal n-type silicon rectangular cantilevers with square pyramidal tips of radii <10 nm for contact and tapping mode (tapping-mode etched silicon probe or TESP) AFMs are commercially available from Digital Instruments and Nanosensors GmbH, Aidlingen, Germany (Figs. 2.15b and 2.16). Spring constants and resonant frequencies are also presented in the Fig. 2.15b.

Commercial triangular Si_3N_4 cantilevers have a typical width:thickness ratio of 10 to 30, which results in spring constants that are 100–1000 times stiffer in the lateral direction than in the normal direction. Therefore, these cantilevers are not well suited for torsion. For friction measurements, the torsional spring constant should be minimized in order to be sensitive to the lateral force. Rather long

Table 2.4 Vertical (k_z), lateral (k_y), and torsional (k_{yT}) spring constants of rectangular cantilevers made of Si (IBM) and PECVD Si_3N_4 (source: Veeco Instruments, Inc.)

Dimensions/stiffness	Si cantilever	Si_3N_4 cantilever
Length L (μm)	100	100
Width b (μm)	10	20
Thickness h (μm)	1	0.6
Tip length (μm)	5	3
k_z (N/m)	0.4	0.15
k_y (N/m)	40	175
k_{yT} (N/m)	120	116
ω_0 (kHz)	≈90	≈ 65

Note: $k_z = Ebh^3/(4L^3)$, $k_y = Eb^3h/(4\ell^3)$, $k_{yT} = Gbh^3/(3L\ell^2)$, and $\omega_0 = [k_z/(m_c + 0.24bhL\rho)]^{1/2}$, where E is Young's modulus, G is the modulus of rigidity [$= E/2(1 + \nu)$, ν is Poisson's ratio], ρ is the mass density of the cantilever, and m_c is the concentrated mass of the tip (≈4 ng) [94]. For Si, $E = 130$ GPa, $\rho g = 2{,}300$ kg/m^3, and $\nu = 0.3$. For Si_3N_4, $E = 150$ GPa, $\rho g = 3{,}100$ kg/m^3, and $\nu = 0.3$

cantilevers with small thicknesses and large tip lengths are most suitable. Rectangular beams have smaller torsional spring constants than the triangular (V-shaped) cantilevers. Table 2.4 lists the spring constants (with the full length of the beam used) in three directions for typical rectangular beams. We note that the lateral and torsional spring constants are about two orders of magnitude larger than the normal spring constants. A cantilever beam required for the tapping mode is quite stiff and may not be sensitive enough for friction measurements. Meyer et al. [140] used a specially designed rectangular silicon cantilever with length = 200 μm, width = 21 μm, thickness = 0.4 μm, tip length = 12.5 μm and shear modulus = 50 GPa, giving a normal spring constant of 0.007 N/m and a torsional spring constant of 0.72 N/m, which gives a lateral force sensitivity of 10 pN and an angle of resolution of 10^{-7} rad. Using this particular geometry, the sensitivity to lateral forces can be improved by about a factor of 100 compared with commercial V-shaped Si_3N_4 or the rectangular Si or Si_3N_4 cantilevers used by Meyer and Amer [8], with torsional spring constants of ≈100 N/m. Ruan and Bhushan [136] and Bhushan and Ruan [9] used 115 μm long, wide-legged V-shaped cantilevers made of Si_3N_4 for friction measurements.

For scratching, wear and indentation studies, single-crystal natural diamond tips ground to the shape of a three-sided pyramid with an apex angle of either 60° or 80° and a point sharpened to a radius of about 100 nm are commonly used [4, 10] (Figs. 2.15c and 2.16). The tips are bonded with conductive epoxy to a gold-plated 304 stainless steel spring sheet (length = 20 mm, width = 0.2 mm, thickness = 20–60 μm) which acts as a cantilever. The free length of the spring is varied in order to change the beam stiffness. The normal spring constant of the beam ranges from about 5 to 600 N/m for a 20 μm thick beam. The tips are produced by R-DEC Co., Tsukuba, Japan.

High aspect ratio tips are used to image within trenches. Examples of two probes used are shown in Fig. 2.17. These high aspect ratio tip (HART) probes are

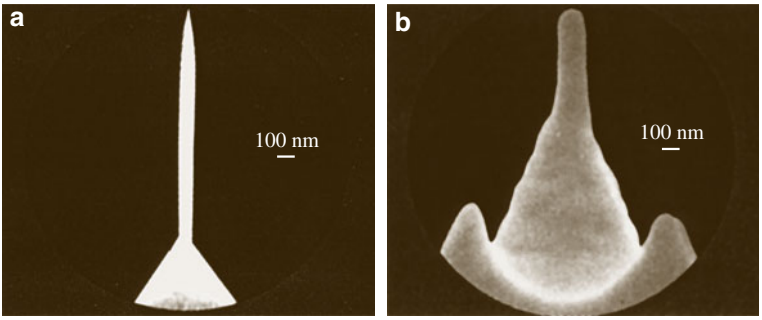

Fig. 2.17 Schematics of **(a)** HART Si_3N_4 probe, and **(b)** an FIB-milled Si_3N_4 probe

produced from conventional Si_3N_4 pyramidal probes. Through a combination of focused ion beam (FIB) and high-resolution scanning electron microscopy (SEM) techniques, a thin filament is grown at the apex of the pyramid. The probe filament is ≈1 μm long and 0.1 μm in diameter. It tapers to an extremely sharp point (with a radius that is better than the resolutions of most SEMs). The long thin shape and sharp radius make it ideal for imaging within *vias* of microstructures and trenches (>0.25 μm). This is, however, unsuitable for imaging structures at the atomic level, since probe flexing can create image artefacts. A FIB-milled probe is used for atomic-scale imaging, which is relatively stiff yet allows for closely spaced topography. These probes start out as conventional Si_3N_4 pyramidal probes, but the pyramid is FIB-milled until a small cone shape is formed which has a high aspect ratio and is 0.2–0.3 μm in length. The milled probes permit nanostructure resolution without sacrificing rigidity. These types of probes are manufactured by various manufacturers including Materials Analytical Services.

Carbon nanotube tips with small diameters and high aspect ratios are used for high-resolution imaging of surfaces and of deep trenches, in the tapping mode or the noncontact mode. Single-wall carbon nanotubes (SWNTs) are microscopic graphitic cylinders that are 0.7–3 nm in diameter and up to many microns in length. Larger structures called multiwall carbon nanotubes (MWNTs) consist of nested, concentrically arranged SWNTs and have diameters of 3–50 nm. MWNT carbon nanotube AFM tips are produced by manual assembly [141], chemical vapor deposition (CVD) synthesis, and a hybrid fabrication process [142]. Figure 2.18 shows a TEM micrograph of a carbon nanotube tip, ProbeMax, commercially produced by mechanical assembly by Piezomax Technologies, Inc. (Middleton, USA). To fabricate these tips, MWNTs are produced using a carbon arc and they are physically attached to the single-crystal silicon, square-pyramidal tips in the SEM, using a manipulator and the SEM stage to independently control the nanotubes and the tip. When the nanotube is first attached to the tip, it is usually too long to image with. It is shortened by placing it in an AFM and applying voltage between the tip and the sample. Nanotube tips are also commercially produced by CVD synthesis by NanoDevices (Santa Barbara, USA).

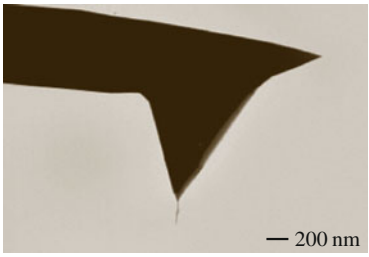

Fig. 2.18 SEM micrograph of a multiwall carbon nanotube (MWNT) tip physically attached to a single-crystal silicon, square-pyramidal tip (Courtesy of Piezomax Technologies, Inc.)

2.2.4 Friction Measurement Methods

The two methods for performing friction measurements that are based on the work by Ruan and Bhushan [136] are now described in more detail (also see [8]). The scanning angle is defined as the angle relative to the y-axis in Fig. 2.19a. This is also the long axis of the cantilever. The zero-degree scanning angle corresponds to the sample scan in the y-direction, and the 90° scanning angle corresponds to the sample scan perpendicular to this axis in the x–y-plane (along x-axis). If both the y- and $-y$-directions are scanned, we call this a *parallel scan*. Similarly, a *perpendicular scan* means that both the x- and $-x$-directions are scanned. The direction of sample travel for each of these two methods is illustrated in Fig. 2.19b.

Using method 1 (*height* mode with parallel scans) in addition to topographic imaging, it is also possible to measure friction force when the sample scanning direction is parallel to the y-direction (parallel scan). If there was no friction force between the tip and the moving sample, the topographic feature would be the only factor that would cause the cantilever to be deflected vertically. However, friction force does exist on all surfaces that are in contact where one of the surfaces is moving relative to the other. The friction force between the sample and the tip will also cause the cantilever to be deflected. We assume that the normal force between the sample and the tip is W_0 when the sample is stationary (W_0 is typically 10–200 nN), and the friction force between the sample and the tip is W_f as the sample is scanned by the tip. The direction of the friction force (W_f) is reversed as the scanning direction of the sample is reversed from the positive (y) to the negative ($-y$) direction ($W_{f(y)} = -W_{f(-y)}$).

When the vertical cantilever deflection is set at a constant level, it is the total force (normal force and friction force) applied to the cantilever that keeps the cantilever deflection at this level. Since the friction force is directed in the opposite direction to the direction of travel of the sample, the normal force will have to be adjusted accordingly when the sample reverses its traveling direction, so that the total deflection of the cantilever will remain the same. We can calculate the difference in the normal force between the two directions of travel for a given

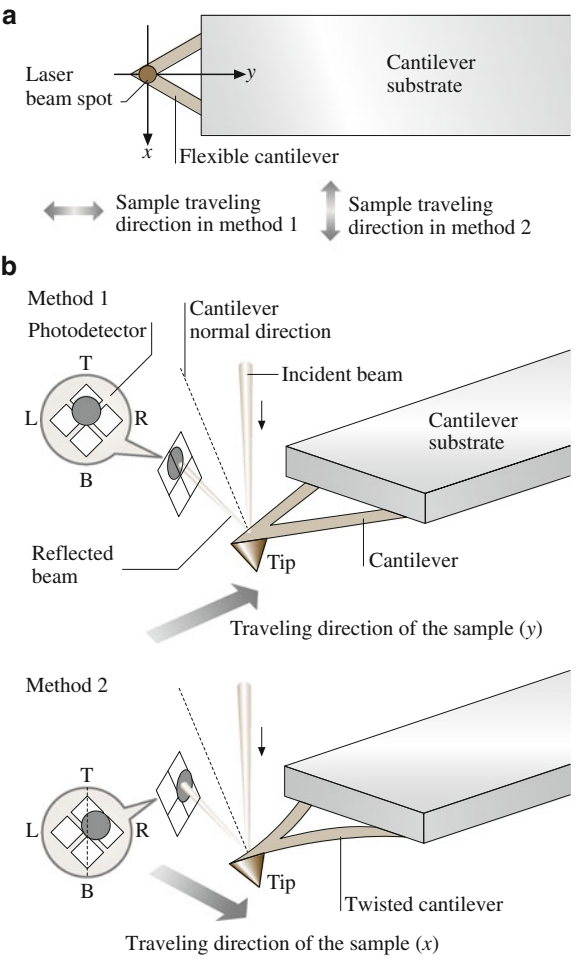

Fig. 2.19 **(a)** Schematic defining the *x*- and *y*-directions relative to the cantilever, and showing the direction of sample travel in two different measurement methods discussed in the text. **(b)** Schematic of deformation of the tip and cantilever shown as a result of sliding in the *x*- and *y*-directions. A twist is introduced to the cantilever if the scanning is performed in the *x*-direction ((**b**), *lower part*) (After [136])

friction force W_f. First, since the deflection is constant, the total moment applied to the cantilever is constant. If we take the reference point to be the point where the cantilever joins the cantilever holder (substrate), point P in Fig. 2.20, we have the following relationship

$$(W_0 - \Delta W_1)L + W_f \ell = (W_0 + \Delta W_2)L - W_f \ell \tag{2.1}$$

or

$$(\Delta W_1 + \Delta W_2)L = 2W_f \ell. \tag{2.2}$$

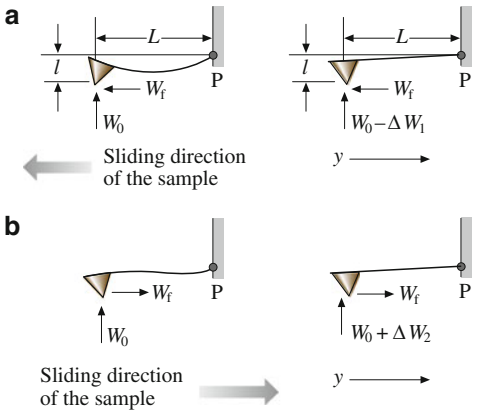

Fig. 2.20 **(a)** Schematic showing an additional bending of the cantilever due to friction force when the sample is scanned in the y- or $-y$-directions (*left*). **(b)** This effect can be canceled out by adjusting the piezo height using a feedback circuit (*right*) (After [136])

Thus

$$W_f = (\Delta W_1 + \Delta W_2)L/(2\ell), \tag{2.3}$$

where ΔW_1 and ΔW_2 are the absolute values of the changes in normal force when the sample is traveling in the $-y$- and y-directions, respectively, as shown in Fig. 2.20; L is the length of the cantilever; ℓ is the vertical distance between the end of the tip and point P. The coefficient of friction (μ) between the tip and the sample is then given as

$$\mu = \frac{W_f}{W_0} = \left(\frac{(\Delta W_1 + \Delta W_2)}{W_0}\right)\left(\frac{L}{2\ell}\right). \tag{2.4}$$

There are adhesive and interatomic attractive forces between the cantilever tip and the sample at all times. The adhesive force can be due to water from the capillary condensation and other contaminants present at the surface, which form meniscus bridges [4, 143, 144] and the interatomic attractive force includes van der Waals attractions [18]. If these forces (and the effect of indentation too, which is usually small for rigid samples) can be neglected, the normal force W_0 is then equal to the initial cantilever deflection H_0 multiplied by the spring constant of the cantilever. ($\Delta W_1 + \Delta W_2$) can be derived by multiplying the same spring constant by the change in height of the piezo tube between the two traveling directions (y- and $-y$-directions) of the sample. This height difference is denoted as ($\Delta H_1 + \Delta H_2$), shown schematically in Fig. 2.21. Thus, (2.4) can be rewritten as

$$\mu = \frac{W_f}{W_0} = \left(\frac{(\Delta H_1 + \Delta H_2)}{H_0}\right)\left(\frac{L}{2\ell}\right). \tag{2.5}$$

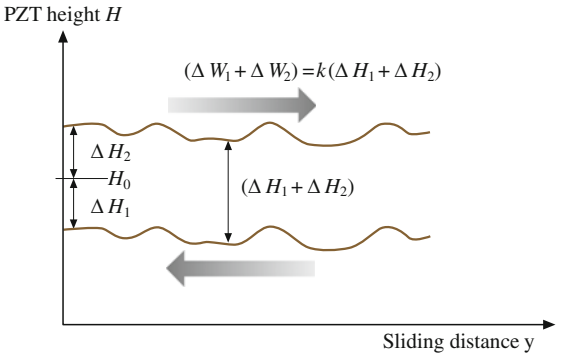

Fig. 2.21 Schematic illustration of the height difference for the piezoelectric tube scanner as the sample is scanned in the y- and $-y$-directions

Since the vertical position of the piezo tube is affected by the topographic profile of the sample surface in addition to the friction force being applied at the tip, this difference must be found point-by-point at the same location on the sample surface, as shown in Fig. 2.21. Subtraction of point-by-point measurements may introduce errors, particularly for rough samples. We will come back to this point later. In addition, precise measurements of L and ℓ (which should include the cantilever angle) are also required.

If the adhesive force between the tip and the sample is large enough that it cannot be neglected, it should be included in the calculation. However, determinations of this force can involve large uncertainties, which is introduced into (2.5). An alternative approach is to make the measurements at different normal loads and to use $\Delta(H_0)$ and $\Delta(\Delta H_1 + \Delta H_2)$ in (2.5). Another comment on (2.5) is that, since only the ratio between $(\Delta H_1 + \Delta H_2)$ and H_0 enters this equation, the vertical position of the piezo tube H_0 and the difference in position $(\Delta H_1 + \Delta H_2)$ can be in volts as long as the vertical travel of the piezo tube and the voltage applied to have a linear relationship. However, if there is a large nonlinearity between the piezo tube traveling distance and the applied voltage, this nonlinearity must be included in the calculation.

It should also be pointed out that (2.4) and (2.5) are derived under the assumption that the friction force W_f is the same for the two scanning directions of the sample. This is an approximation, since the normal force is slightly different for the two scans and the friction may be direction-dependent. However, this difference is much smaller than W_0 itself. We can ignore the second-order correction.

Method 2 (*aux* mode with perpendicular scan) of measuring friction was suggested by Meyer and Amer [8]. The sample is scanned perpendicular to the long axis of the cantilever beam (along the x- or $-x$-direction in Fig. 2.19a) and the outputs from the two horizontal quadrants of the photodiode detector are measured. In this arrangement, as the sample moves under the tip, the friction force will cause the cantilever to twist. Therefore, the light intensity between the left and right (L and R in Fig. 2.19b, right) detectors will be different. The differential signal

between the left and right detectors is denoted the FFM signal [(L − R)/(L + R)]. This signal can be related to the degree of twisting, and hence to the magnitude of friction force. Again, because possible errors in measurements of the normal force due to the presence of adhesive force at the tip–sample interface, the slope of the friction data (FFM signal versus normal load) needs to be measured for an accurate value of the coefficient of friction.

While friction force contributes to the FFM signal, friction force may not be the only contributing factor in commercial FFM instruments (for example, NanoScope IV). One can see this if we simply engange the cantilever tip with the sample. The left and right detectors can be balanced beforehand by adjusting the positions of the detectors so that the intensity difference between these two detectors is zero (FFM signal is zero). Once the tip is engaged with the sample, this signal is no longer zero, even if the sample is not moving in the *x*–*y*-plane with no friction force applied. This would be a detrimental effect. It has to be understood and eliminated from the data acquisition before any quantitative measurement of friction force is made.

One of the reasons for this observation is as follows. The detectors may not have been properly aligned with respect to the laser beam. To be precise, the vertical axis of the detector assembly (the line joining T–B in Fig. 2.22) is not in the plane defined by the incident laser beam and the beam reflected from the untwisted cantilever (we call this plane the *beam plane*). When the cantilever vertical deflection changes due to a change in the normal force applied (without the sample being scanned in the *x*–*y*-plane), the laser beam will be reflected up and down and form a projected trajectory on the detector. (Note that this trajectory is

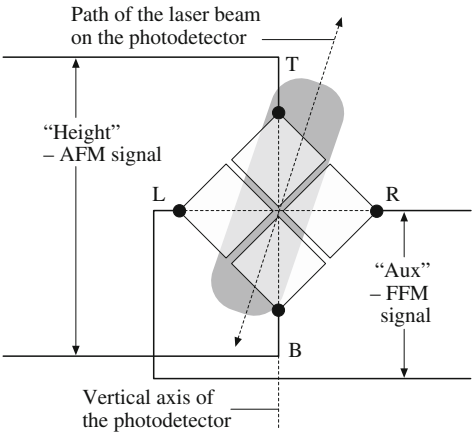

Fig. 2.22 The trajectory of the laser beam on the photodetectors as the cantilever is vertically deflected (with no torsional motion) with respect to the laser beam for a misaligned photodetector. For a change of normal force (vertical deflection of the cantilever), the laser beam is projected to a different position on the detector. Due to a misalignment, the projected trajectory of the laser beam on the detector is not parallel with the detector vertical axis (the line T–B) (After [136])

in the defined beam plane.) If this trajectory is not coincident with the vertical axis of the detector, the laser beam will not evenly bisect the left and right quadrants of the detectors, even under the condition of no torsional motion of the cantilever (Fig. 2.22). Thus, when the laser beam is reflected up and down due a change in the normal force, the intensity difference between the left and right detectors will also change. In other words, the FFM signal will change as the normal force applied to the tip is changed, even if the tip is not experiencing any friction force. This (FFM) signal is unrelated to friction force or to the actual twisting of the cantilever. We will call this part of the FFM signal $\mathrm{FFM_F}$, and the part which is truly related to friction force $\mathrm{FFM_T}$.

The $\mathrm{FFM_F}$ signal can be eliminated. One way of doing this is as follows. First the sample is scanned in both the x- and the $-x$-directions and the FFM signals for scans in each direction are recorded. Since the friction force reverses its direction of action when the scanning direction is reversed from the x- to the $-x$-direction, the $\mathrm{FFM_T}$ signal will change signs as the scanning direction of the sample is reversed ($\mathrm{FFM_T}(x) = -\mathrm{FFM_T}(-x)$). Hence the $\mathrm{FFM_T}$ signal will be canceled out if we take the sum of the FFM signals for the two scans. The average value of the two scans will be related to $\mathrm{FFM_F}$ due to the misalignment,

$$\mathrm{FFM}(x) + \mathrm{FFM}(-x) = 2\mathrm{FFM_F}. \tag{2.6}$$

This value can therefore be subtracted from the original FFM signals of each of these two scans to obtain the true FFM signal ($\mathrm{FFM_T}$). Or, alternately, by taking the difference of the two FFM signals, one gets the $\mathrm{FFM_T}$ value directly

$$\mathrm{FFM}(x) - \mathrm{FFM}(-x) = \mathrm{FFM_T}(x) - \mathrm{FFM_T}(-x) = 2\mathrm{FFM_T}(x). \tag{2.7}$$

Ruan and Bhushan [136] have shown that the error signal ($\mathrm{FFM_F}$) can be very large compared to the friction signal $\mathrm{FFM_T}$, so correction is required.

Now we compare the two methods. The method of using the *height* mode and parallel scanning (method 1) is very simple to use. Technically, this method can provide 3-D friction profiles and the corresponding topographic profiles. However, there are some problems with this method. Under most circumstances, the piezo scanner displays hysteresis when the traveling direction of the sample is reversed. Therefore, the measured surface topographic profiles will be shifted relative to each other along the y-axis for the two opposite (y and $-y$) scans. This would make it difficult to measure the local difference in height of the piezo tube for the two scans. However, the average difference in height between the two scans and hence the average friction can still be measured. The measurement of average friction can serve as an internal means of friction force calibration. Method 2 is a more desirable approach. The subtraction of the $\mathrm{FFM_F}$ signal from FFM for the two scans does not introduce any error into local friction force data. An ideal approach when using this method would be to add the average values of the two profiles in order to get the error component ($\mathrm{FFM_F}$) and then subtract this component from either profile to get true friction profiles in either directions. By performing measurements at various

loads, we can get the average value of the coefficient of friction which then can be used to convert the friction profile to the coefficient of friction profile. Thus, any directionality and local variations in friction can be easily measured. In this method, since topography data are not affected by friction, accurate topography data can be measured simultaneously with friction data and a better localized relationship between the two can be established.

2.2.5 *Normal Force and Friction Force Calibrations of Cantilever Beams*

Based on Ruan and Bhushan [136], we now discuss normal force and friction force calibrations. In order to calculate the absolute values of normal and friction forces in Newtons using the measured AFM and FFM_T voltage signals, it is necessary to first have an accurate value of the spring constant of the cantilever (k_c). The spring constant can be calculated using the geometry and the physical properties of the cantilever material [8, 94, 137]. However, the properties of the PECVD Si_3N_4 (used to fabricate cantilevers) can be different from those of the bulk material. For example, using ultrasonics, we found the Young's modulus of the cantilever beam to be about 238 ± 18 GPa, which is less than that of bulk Si_3N_4 (310 GPa). Furthermore, the thickness of the beam is nonuniform and difficult to measure precisely. Since the stiffness of a beam goes as the cube of thickness, minor errors in precise measurements of thickness can introduce substantial stiffness errors. Thus one should measure the spring constant of the cantilever experimentally. Cleveland et al. [145] measured normal spring constants by measuring resonant frequencies of beams.

For normal spring constant measurement, Ruan and Bhushan [136] used a stainless steel spring sheet of known stiffness (width = 1.35 mm, thickness = 15 μm, free hanging length = 5.2 mm). One end of the spring was attached to the sample holder and the other end was made to contact with the cantilever tip during the measurement (Fig. 2.23). They measured the piezo travel for a given cantilever deflection. For a rigid sample (such as diamond), the piezo travel Z_t (measured from the point where the tip touches the sample) should equal the cantilever deflection. To maintain the cantilever deflection at the same level using a flexible spring sheet, the new piezo travel $Z_{t'}$ would need to be different from Z_t. The difference between $Z_{t'}$ and Z_t corresponds to the deflection of the spring sheet. If the spring constant of the spring sheet is k_s, the spring constant of the cantilever k_c can be calculated by

$$(Z_{t'} - Z_t)k_s = Z_t k_c$$

or

$$k_c = k_s(Z_{t'} - Z_t)/Z_t. \tag{2.8}$$

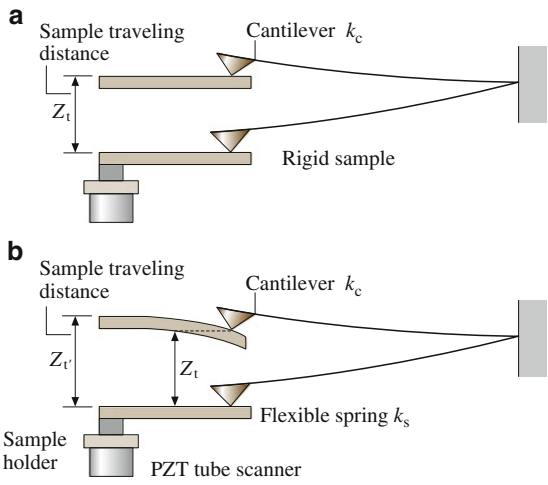

Fig. 2.23 Illustration showing the deflection of the cantilever as it is pushed by **(a)** a rigid sample, **(b)** a flexible spring sheet (After [136])

The spring constant of the spring sheet (k_s) used in this study is calculated to be 1.54 N/m. For the wide-legged cantilever used in our study (length = 115 μm, base width = 122 μm, leg width = 21 μm and thickness = 0.6 μm), k_c was measured to be 0.40 N/m instead of the 0.58 N/m reported by its manufacturer – Digital Instruments, Inc. To relate the photodiode detector output to the cantilever deflection in nanometers, they used the same rigid sample to push against the AFM tip. Since the cantilever vertical deflection equals the sample traveling distance measured from the point where the tip touches the sample for a rigid sample, the photodiode output observed as the tip is pushed by the sample can be converted directly to the cantilever deflection. For these measurements, they found the conversion factor to be 20 nm/V.

The normal force applied to the tip can be calculated by multiplying the cantilever vertical deflection by the cantilever spring constant for samples that have very small adhesion with the tip. If the adhesive force between the sample and the tip is large, it should be included in the normal force calculation. This is particularly important in atomic-scale force measurements, because the typical normal force that is measured in this region is in the range of a few hundreds of nN to a few mN. The adhesive force could be comparable to the applied force.

The conversion of friction signal (from FFM_T) to friction force is not as straightforward. For example, one can calculate the degree of twisting for a given friction force using the geometry and the physical properties of the cantilever [53, 144]. One would need information about the detector such as its quantum efficiency, laser power, gain and so on in order to be able convert the signal into the degree of twisting. Generally speaking, this procedure can not be accomplished without having some detailed information about the instrument. This information is not usually provided by the manufacturer. Even if this information is readily available, errors may still occur when using this approach because there will always be variations as a result of the instrumental set-up. For example, it has been noticed that the measured FFM_T signal varies for the same sample when different AFM microscopes from the same manufacturer are used. This means that one can not

calibrate the instrument experimentally using this calculation. O'Shea et al. [144] did perform a calibration procedure in which the torsional signal was measured as the sample was displaced a known distance laterally while ensuring that the tip did not slide over the surface. However, it is difficult to verify that tip sliding does not occur.

A new method of calibration is therefore required. There is a simpler, more direct way of doing this. The first method described above (method 1) of measuring friction can provide an absolute value of the coefficient of friction directly. It can therefore be used as an internal calibration technique for data obtained using method 2. Or, for a polished sample, which introduces the least error into friction measurements taken using method 1, method 1 can be used to calibrate the friction force for method 2. Then this calibration can be used for measurements taken using method 2. In method 1, the length of the cantilever required can be measured using an optical microscope; the length of the tip can be measured using a scanning electron microscope. The relative angle between the cantilever and the horizontal sample surface can be measured directly. This enables the coefficient of friction to be measured with few unknown parameters. The friction force can then be calculated by multiplying the coefficient of friction by the normal load. The FFM_T signal obtained using method 2 is then converted into the friction force. For their instrument, they found the conversion to be 8.6 nN/V.

2.3 AFM Instrumentation and Analyses

The performance of AFMs and the quality of AFM images greatly depend on the instrument available and the probes (cantilever and tips) in use. This section describes the mechanics of cantilevers, instrumentation and analysis of force detection systems for cantilever deflections, and scanning and control systems.

2.3.1 The Mechanics of Cantilevers

Stiffness and Resonances of Lumped Mass Systems

All of the building blocks of an AFM, including the body of the microscope itself and the force-measuring cantilevers, are mechanical resonators. These resonances can be excited either by the surroundings or by the rapid movement of the tip or the sample. To avoid problems due to building- or air-induced oscillations, it is of paramount importance to optimize the design of the AFM for high resonant frequencies. This usually means decreasing the size of the microscope [146]. By using cube-like or sphere-like structures for the microscope, one can considerably increase the lowest eigenfrequency. The fundamental natural frequency ω_0 of any spring is given by

$$\omega_0 = \frac{1}{2\pi}\sqrt{\frac{k}{m_{\text{eff}}}}, \tag{2.9}$$

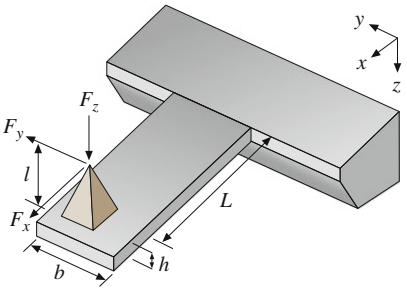

Fig. 2.24 A typical AFM cantilever with length L, width b, and height h. The height of the tip is ℓ. The material is characterized by the Young's modulus E, the shear modulus G and the mass density ρ. Normal (F_z), axial (F_x) and lateral (F_y) forces exist at the end of the tip

where k is the spring constant (stiffness) in the normal direction and m_{eff} is the effective mass. The spring constant k of a cantilever beam with uniform cross section (Fig. 2.24) is given by [147]

$$k = \frac{3EI}{L^3}, \tag{2.10}$$

where E is the Young's modulus of the material, L is the length of the beam and I is the moment of inertia of the cross section. For a rectangular cross section with a width b (perpendicular to the deflection) and a height h one obtains the following expression for I

$$I = \frac{bh^3}{12}. \tag{2.11}$$

Combining (2.9)–(2.11), we get an expression for ω_0

$$\omega_0 = \sqrt{\frac{Ebh^3}{4L^3 m_{\text{eff}}}}. \tag{2.12}$$

The effective mass can be calculated using Raleigh's method. The general formula using Raleigh's method for the kinetic energy T of a bar is

$$T = \frac{1}{2}\int_0^L \frac{m}{L}\left(\frac{\partial z(x)}{\partial t}\right)^2 \mathrm{d}x. \tag{2.13}$$

For the case of a uniform beam with a constant cross section and length L, one obtains for the deflection $z(x) = z_{\max}[1 - (3x/2L) + (x^3/2L^3)]$ Inserting $z_{\max}$ into (2.13) and solving the integral gives

$$T = \frac{1}{2}\int_0^L \frac{m}{L}\left[\frac{\partial z_{\max}(x)}{\partial t}\left(1 - \frac{3x}{2L}\right) + \left(\frac{x^3}{L^3}\right)\right]^2 \mathrm{d}x = \frac{1}{2} m_{\text{eff}} (z_{\max} t)^2,$$

which gives

$$m_{\text{eff}} = \frac{9}{20}m. \tag{2.14}$$

Substituting (2.14) into (2.12) and noting that $m = \rho Lbh$, where ρ is the mass density, one obtains the following expression

$$\omega_0 = \left(\frac{\sqrt{5}}{3}\sqrt{\frac{\mathrm{E}}{\rho}}\right)\frac{h}{L^2}. \tag{2.15}$$

It is evident from (2.15) that one way to increase the natural frequency is to choose a material with a high ratio E/ρ; see Table 2.2 for typical values of $\sqrt{E/\rho}$ for various commonly used materials. Another way to increase the lowest eigenfrequency is also evident in (2.15). By optimizing the ratio h/L^2, one can increase the resonant frequency. However, it does not help to make the length of the structure smaller than the width or height. Their roles will just be interchanged. Hence the optimum structure is a cube. This leads to the design rule that long, thin structures like sheet metal should be avoided. For a given resonant frequency, the quality factor Q should be as low as possible. This means that an inelastic medium such as rubber should be in contact with the structure in order to convert kinetic energy into heat.

Stiffness and Resonances of Cantilevers

Cantilevers are mechanical devices specially shaped to measure tiny forces. The analysis given in the previous section is applicable. However, to better understand the intricacies of force detection systems, we will discuss the example of a cantilever beam with uniform cross section (Fig. 2.24). The bending of a beam due to a normal load on the beam is governed by the Euler equation [147]

$$M = EI(x)\frac{\mathrm{d}^2 z}{\mathrm{d}x^2}, \tag{2.16}$$

where M is the bending moment acting on the beam cross section. $I(x)$ is the moment of inertia of the cross section with respect to the neutral axis, defined by

$$I(x) = \iint_{z\ y} z^2\,\mathrm{d}y\mathrm{d}z. \tag{2.17}$$

For a normal force F_z acting at the tip,

$$M(x) = (L - x)F_z \tag{2.18}$$

since the moment must vanish at the endpoint of the cantilever. Integrating (2.16) for a normal force F_z acting at the tip and observing that EI is a constant for beams with a uniform cross section, one gets

$$z(x) = \frac{L^3}{6EI}\left(\frac{x}{L}\right)^2\left(3 - \frac{x}{L}\right)F_z. \tag{2.19}$$

The slope of the beam is

$$z'(x) = \frac{Lx}{2EI}\left(2 - \frac{x}{L}\right)F_z. \tag{2.20}$$

From (2.19) and (2.20), at the end of the cantilever (for $x = L$), for a rectangular beam, and by using an expression for I in (2.11), one gets

$$z(L) = \frac{4}{Eb}\left(\frac{L}{h}\right)^3 F_z, \tag{2.21}$$

$$z'(L) = \frac{3}{2}\left(\frac{z}{L}\right). \tag{2.22}$$

Now, the stiffness in the normal (z) direction k_z is

$$k_z = \frac{F_z}{z(L)} = \frac{Eb}{4}\left(\frac{h}{L}\right)^3. \tag{2.23}$$

and the change in angular orientation of the end of cantilever beam is

$$\Delta\alpha = \frac{3}{2}\frac{z}{L} = \frac{6}{Ebh}\left(\frac{L}{h}\right)^2 F_z. \tag{2.24}$$

Now we ask what will, to a first-order approximation, happen if we apply a lateral force F_y to the end of the tip (Fig. 2.24). The cantilever will bend sideways and it will twist. The stiffness in the lateral (y) direction k_y can be calculated with (2.23) by exchanging b and h

$$k_y = \frac{Eh}{4}\left(\frac{b}{L}\right)^3. \tag{2.25}$$

Therefore, the bending stiffness in the lateral direction is larger than the stiffness for bending in the normal direction by $(b/h)^2$. The twisting or torsion on the other hand is more complicated to handle. For a wide, thin cantilever ($b \gg h$) we obtain torsional stiffness along y-axis $k_{y\mathrm{T}}$

$$k_{y\mathrm{T}} = \frac{Gbh^3}{3L\ell^2}, \tag{2.26}$$

where G is the modulus of rigidity ($= E/2(1 + \nu)$; ν is Poisson's ratio). The ratio of the torsional stiffness to the lateral bending stiffness is

$$\frac{k_{y\mathrm{T}}}{k_y} = \frac{1}{2}\left(\frac{\ell b}{hL}\right)^2, \tag{2.27}$$

where we assume $\nu = 0.333$. We see that thin, wide cantilevers with long tips favor torsion while cantilevers with square cross sections and short tips favor bending. Finally, we calculate the ratio between the torsional stiffness and the normal bending stiffness,

$$\frac{k_{y\mathrm{T}}}{k_z} = 2\left(\frac{L}{\ell}\right)^2. \tag{2.28}$$

Equations (2.26)–(2.28) hold in the case where the cantilever tip is exactly in the middle axis of the cantilever. Triangular cantilevers and cantilevers with tips which are not on the middle axis can be dealt with by finite element methods.

The third possible deflection mode is the one from the force on the end of the tip along the cantilever axis, F_x (Fig. 2.24). The bending moment at the free end of the cantilever is equal to $F_x\ell$. This leads to the following modification of (2.18) for forces F_z and F_x

$$M(x) = (L - x)F_z + F_x\ell. \tag{2.29}$$

Integration of (2.16) now leads to

$$z(x) = \frac{1}{2EI}\left[Lx^2\left(1 - \frac{x}{3L}\right)F_z + \ell x^2 F_x\right] \tag{2.30}$$

and

$$z'(x) = \frac{1}{EI}\left[\frac{Lx}{2}\left(2 - \frac{x}{L}\right)F_z + \ell x F_x\right]. \tag{2.31}$$

Evaluating (2.30) and (2.31) at the end of the cantilever, we get the deflection and the tilt

$$\begin{aligned} z(L) &= \frac{L^2}{EI}\left(\frac{L}{3}F_z - \frac{\ell}{2}F_x\right), \\ z'(L) &= \frac{L}{EI}\left(\frac{L}{2}F_z + \ell F_x\right). \end{aligned} \tag{2.32}$$

From these equations, one gets

$$\begin{aligned} F_z &= \frac{12EI}{L^3}\left[z(L) - \frac{Lz'(L)}{2}\right], \\ F_x &= \frac{2EI}{\ell L^2}[2Lz'(L) - 3z(L)]. \end{aligned} \tag{2.33}$$

A second class of interesting properties of cantilevers is their resonance behavior. For cantilever beams, one can calculate the resonant frequencies [147, 148]

$$\omega_n^{\text{free}} = \frac{\lambda_n^2}{2\sqrt{3}} \frac{h}{L^2} \sqrt{\frac{E}{\rho}} \tag{2.34}$$

with $\lambda_0 = (0.596864\ldots)\pi$, $\lambda_1 = (1.494175\ldots)\pi$, $\lambda_n \to (n + 1/2)\pi$. The subscript n represents the order of the frequency, such as the fundamental, the second mode, and the nth mode.

A similar equation to (2.34) holds for cantilevers in rigid contact with the surface. Since there is an additional restriction on the movement of the cantilever, namely the location of its endpoint, the resonant frequency increases. Only the terms of λ_n change to [148]

$$\lambda_0' = (1.2498763\ldots)\pi, \quad \lambda_1' = (2.2499997\ldots)\pi, \quad \lambda_n' \to (n + 1/4)\pi. \tag{2.35}$$

The ratio of the fundamental resonant frequency during contact to the fundamental resonant frequency when not in contact is 4.3851.

For the torsional mode we can calculate the resonant frequencies as

$$\omega_0^{\text{tors}} = 2\pi \frac{h}{Lb} \sqrt{\frac{G}{\rho}}. \tag{2.36}$$

For cantilevers in rigid contact with the surface, we obtain the following expression for the fundamental resonant frequency [148]

$$\omega_0^{\text{tors,contact}} = \frac{\omega_0^{\text{tors}}}{\sqrt{1 + 3(2L/b)^2}}. \tag{2.37}$$

The amplitude of the thermally induced vibration can be calculated from the resonant frequency using

$$\Delta z_{\text{therm}} = \sqrt{\frac{k_B T}{k}}, \tag{2.38}$$

where k_B is Boltzmann's constant and T is the absolute temperature. Since AFM cantilevers are resonant structures, sometimes with rather high Q values, the thermal noise is not as evenly distributed as (2.38) suggests. The spectral noise density below the peak of the response curve is [148]

$$z_0 = \sqrt{\frac{4k_B T}{k\omega_0 Q}} \quad (\text{in m}/\sqrt{\text{Hz}}), \tag{2.39}$$

where Q is the quality factor of the cantilever, described earlier.

2.3.2 *Instrumentation and Analyses of Detection Systems for Cantilever Deflections*

A summary of selected detection systems was provided in Fig. 2.8. Here we discuss the pros and cons of various systems in detail.

Optical Interferometer Detection Systems

Soon after the first papers on the AFM [2] appeared, which used a tunneling sensor, an instrument based on an interferometer was published [149]. The sensitivity of the interferometer depends on the wavelength of the light employed in the apparatus. Figure 2.25 shows the principle of such an interferometeric design. The light incident from the left is focused by a lens onto the cantilever. The reflected light is collimated by the same lens and interferes with the light reflected at the flat. To separate the reflected light from the incident light, a $\lambda/4$ plate converts the linearly polarized incident light into circularly polarized light. The reflected light is made linearly polarized again by the $\lambda/4$-plate, but with a polarization orthogonal to that of the incident light. The polarizing beam splitter then deflects the reflected light to the photodiode.

Homodyne Interferometer

To improve the signal-to-noise ratio of the interferometer, the cantilever is driven by a piezo near its resonant frequency. The amplitude Δz of the cantilever as a function of driving frequency Ω is

$$\Delta z(\Omega) = \Delta z_0 \frac{\Omega_0^2}{\sqrt{\left(\Omega^2 - \Omega_0^2\right)^2 + \frac{\Omega^2 \Omega_0^2}{Q^2}}}, \tag{2.40}$$

where Δz_0 is the constant drive amplitude and Ω_0 the resonant frequency of the cantilever. The resonant frequency of the cantilever is given by the effective potential

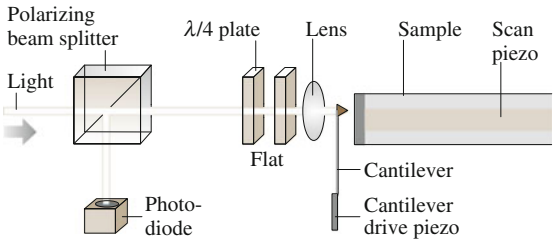

Fig. 2.25 Principle of an interferometric AFM. The light from the laser light source is polarized by the polarizing beam splitter and focused onto the back of the cantilever. The light passes twice through a quarter-wave plate and is hence orthogonally polarized to the incident light. The second arm of the interferometer is formed by the flat. The interference pattern is modulated by the oscillating cantilever

$$\Omega_0 = \sqrt{\left(k + \frac{\partial^2 U}{\partial z^2}\right)\frac{1}{m_{\text{eff}}}}, \tag{2.41}$$

where U is the interaction potential between the tip and the sample. Equation (2.41) shows that an attractive potential decreases Ω_0. The change in Ω_0 in turn results in a change in Δz (2.40). The movement of the cantilever changes the path difference in the interferometer. The light reflected from the cantilever with amplitude $A_{\ell,0}$ and the reference light with amplitude $A_{\text{r},0}$ interfere on the detector. The detected intensity $I(t) = [A_\ell(t) + A_\text{r}(t)]^2$ consists of two constant terms and a fluctuating term

$$2A_\ell(t)A_\text{r}(t) = A_{\ell,0}A_{\text{r},0}\sin\left[\omega t + \frac{4\pi\delta}{\lambda} + \frac{4\pi\Delta z}{\lambda}\sin(\Omega t)\right]\sin(\omega t). \tag{2.42}$$

Here ω is the frequency of the light, λ is the wavelength of the light, δ is the path difference in the interferometer, and Δz is the instantaneous amplitude of the cantilever, given according to (2.40) and (2.41) as a function of Ω, k, and U. The time average of (2.42) then becomes

$$\begin{aligned}\langle 2A_\ell(t)A_\text{r}(t)\rangle_T &\propto \cos\left[\frac{4\pi\delta}{\lambda} + \frac{4\pi\Delta z}{\lambda}\sin(\Omega t)\right] \\ &\approx \cos\left(\frac{4\pi\delta}{\lambda}\right) - \sin\left[\frac{4\pi\Delta z}{\lambda}\sin(\Omega t)\right] \approx \cos\left(\frac{4\pi\delta}{\lambda}\right) - \frac{4\pi\Delta z}{\lambda}\sin(\Omega t).\end{aligned} \tag{2.43}$$

Here all small quantities have been omitted and functions with small arguments have been linearized. The amplitude of Δz can be recovered with a lock-in technique. However, (2.43) shows that the measured amplitude is also a function of the path difference δ in the interferometer. Hence, this path difference δ must be very stable. The best sensitivity is obtained when $\sin(4\delta/\lambda) \approx 0$.

Heterodyne Interferometer

This influence is not present in the heterodyne detection scheme shown in Fig. 2.26. Light incident from the left with a frequency ω is split into a reference path (upper path in Fig. 2.26) and a measurement path. Light in the measurement path is shifted in frequency to $\omega_1 = \omega + \Delta\omega$ and focused onto the cantilever. The cantilever oscillates at the frequency Ω, as in the homodyne detection scheme. The reflected light $A_\ell(t)$ is collimated by the same lens and interferes on the photodiode with the reference light $A_\text{r}(t)$. The fluctuating term of the intensity is given by

$$2A_\ell(t)A_\text{r}(t) = A_{\ell,0}A_{\text{r},0}\sin\left[(\omega + \Delta\omega)t + \frac{4\pi\delta}{\lambda} + \frac{4\pi\Delta z}{\lambda}\sin(\Omega t)\right]\sin(\omega t), \tag{2.44}$$

where the variables are defined as in (2.42). Setting the path difference $\sin(4\pi\delta/\lambda) \approx 0$ and taking the time average, omitting small quantities and linearizing functions with small arguments, we get

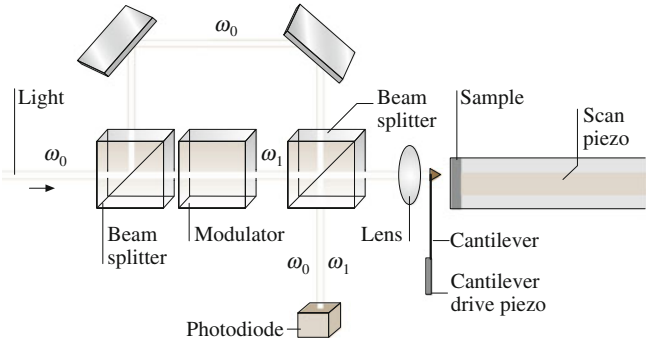

Fig. 2.26 Principle of a heterodyne interferometric AFM. Light with frequency ω_0 is split into a reference path (upper path) and a measurement path. The light in the measurement path is frequency shifted to ω_1 by an acousto-optical modulator (or an electro-optical modulator). The light reflected from the oscillating cantilever interferes with the reference beam on the detector

$$
\begin{aligned}
&\langle 2A_\ell(t)A_\mathrm{r}(t)\rangle_\mathrm{T} \propto \cos\left[\Delta\omega t + \frac{4\pi\delta}{\lambda} + \frac{4\pi\Delta z}{\lambda}\sin(\Omega t)\right] \\
&= \cos\left(\Delta\omega t + \frac{4\pi\delta}{\lambda}\right)\cos\left[\frac{4\pi\Delta z}{\lambda}\sin(\Omega t)\right] - \sin\left(\Delta\omega t + \frac{4\pi\delta}{\lambda}\right)\sin\left[\frac{4\pi\Delta z}{\lambda}\sin(\Omega t)\right] \\
&\approx \cos\left(\frac{4\pi\delta}{\lambda}\right) - \sin\left[\frac{4\pi\Delta z}{\lambda}\sin(\Omega t)\right] \approx \cos\left(\Delta\omega t + \frac{4\pi\delta}{\lambda}\right)\left[1 - \frac{8\pi^2\Delta z^2}{\lambda^2}\sin(\Omega t)\right] \\
&\quad - \frac{4\pi\Delta z}{\lambda}\sin\left(\Delta\omega t + \frac{4\pi\delta}{\lambda}\right)\sin(\Omega t) \\
&= \cos\left(\Delta\omega t + \frac{4\pi\delta}{\lambda}\right) - \frac{8\pi^2\Delta z^2}{\lambda^2}\cos\left(\Delta\omega t + \frac{4\pi\delta}{\lambda}\right) \\
&\quad \times \sin(\Omega t) - \frac{4\pi\Delta z}{\lambda}\sin\left(\Delta\omega t + \frac{4\pi\delta}{\lambda}\right)\sin(\Omega t) \\
&= \cos\left(\Delta\omega t + \frac{4\pi\delta}{\lambda}\right) - \frac{4\pi^2\Delta z^2}{\lambda^2}\cos\left(\Delta\omega t + \frac{4\pi\delta}{\lambda}\right) + \frac{4\pi^2\Delta z^2}{\lambda^2}\cos\left(\Delta\omega t + \frac{4\pi\delta}{\lambda}\right) \\
&\quad \cos(2\Omega t) - \frac{4\pi\Delta z}{\lambda}\sin\left(\Delta\omega t + \frac{4\pi\delta}{\lambda}\right)\sin(\Omega t) \\
&= \cos\left(\Delta\omega t + \frac{4\pi\delta}{\lambda}\right)\left(1 - \frac{4\pi^2\Delta z^2}{\lambda^2}\right) + \frac{2\pi^2\Delta z^2}{\lambda^2}\left\{\cos\left[(\Delta\omega + 2\Omega)t + \frac{4\pi\delta}{\lambda}\right]\right. \\
&\quad \left. + \cos\left[(\Delta\omega - 2\Omega)t + \frac{4\pi\delta}{\lambda}\right]\right\} + \frac{2\pi\Delta z}{\lambda}\left\{\cos\left[(\Delta\omega + \Omega)t + \frac{4\pi\delta}{\lambda}\right]\right. \\
&\quad \left. + \cos\left[(\Delta\omega - \Omega)t + \frac{4\pi\delta}{\lambda}\right]\right\}. \qquad (2.45)
\end{aligned}
$$

Multiplying electronically the components oscillating at $\Delta\omega$ and $\Delta\omega + \Omega$ and rejecting any product except the one oscillating at Ω we obtain

$$\begin{aligned} A &= \frac{2\Delta z}{\lambda}\left(1 - \frac{4\pi^2\Delta z^2}{\lambda^2}\right)\cos\left[(\Delta\omega + 2\Omega)t + \frac{4\pi\delta}{\lambda}\right]\cos\left(\Delta\omega t + \frac{4\pi\delta}{\lambda}\right) \\ &= \frac{\Delta z}{\lambda}\left(1 - \frac{4\pi^2\Delta z^2}{\lambda^2}\right)\left\{\cos\left[(2\Delta\omega + \Omega)t + \frac{8\pi\delta}{\lambda}\right] + \cos(\Omega t)\right\} \\ &\approx \frac{\pi\Delta z}{\lambda}\cos(\Omega t). \end{aligned} \tag{2.46}$$

Unlike in the homodyne detection scheme, the recovered signal is independent from the path difference δ of the interferometer. Furthermore, a lock-in amplifier with the reference set sin ($\Delta\omega t$) can measure the path difference δ independent of the cantilever oscillation. If necessary, a feedback circuit can keep $\delta = 0$.

Fiber-Optical Interferometer

The fiber-optical interferometer [129] is one of the simplest interferometers to build and use. Its principle is sketched in Fig. 2.27. The light of a laser is fed into an optical fiber. Laser diodes with integrated fiber pigtails are convenient light sources. The light is split in a fiber-optic beam splitter into two fibers. One fiber is terminated by index-matching oil to avoid any reflections back into the fiber. The end of the other fiber is brought close to the cantilever in the AFM. The emerging light is partially reflected back into the fiber by the cantilever. Most of the light, however, is lost. This is not a big problem since only 4% of the light is reflected at the end of the fiber, at the glass–air interface. The two reflected light waves interfere with each other. The product is guided back into the fiber coupler and again split into two parts. One half is analyzed by the photodiode. The other half is fed back into the laser. Communications grade laser diodes are sufficiently resistant to feedback to be operated in this environment. They have, however, a bad coherence length, which in this case does not matter, since the optical path difference is in any case no larger than 5 μm. Again the end of the fiber has to be positioned on a piezo drive to set the distance between the fiber and the cantilever to $\lambda(n + 1/4)$.

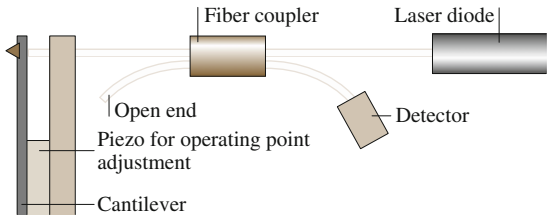

Fig. 2.27 A typical set-up for a fiber-optic interferometer readout

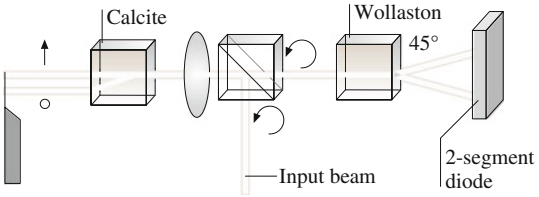

Fig. 2.28 Principle of Nomarski AFM. The circularly polarized input beam is deflected to the left by a nonpolarizing beam splitter. The light is focused onto a cantilever. The calcite crystal between the lens and the cantilever splits the circular polarized light into two spatially separated beams with orthogonal polarizations. The two light beams reflected from the lever are superimposed by the calcite crystal and collected by the lens. The resulting beam is again circularly polarized. A Wollaston prism produces two interfering beams with a $\pi/2$ phase shift between them. The minimal path difference accounts for the excellent stability of this microscope

Nomarski-Interferometer

Another way to minimize the optical path difference is to use the Nomarski interferometer [130]. Figure 2.28 shows a schematic of the microscope. The light from a laser is focused on the cantilever by lens. A birefringent crystal (for instance calcite) between the cantilever and the lens, which has its optical axis 45° off the polarization direction of the light, splits the light beam into two paths, offset by a distance given by the length of the crystal. Birefringent crystals have varying indices of refraction. In calcite, one crystal axis has a lower index than the other two. This means that certain light rays will propagate at different speeds through the crystal than others. By choosing the correct polarization, one can select the ordinary ray or the extraordinary ray or one can get any mixture of the two rays. A detailed description of birefringence can be found in textbooks (e.g., [150]). A calcite crystal deflects the extraordinary ray at an angle of 6° within the crystal. Any separation can be set by choosing a suitable length for the calcite crystal.

The focus of one light ray is positioned near the free end of the cantilever while the other is placed close to the clamped end. Both arms of the interferometer pass through the same space, except for the distance between the calcite crystal and the lever. The closer the calcite crystal is placed to the lever, the less influence disturbances like air currents have.

Sarid [116] has given values for the sensitivities of different interferometeric detection systems. Table 2.5 presents a summary of his results.

Optical Lever

The most common cantilever deflection detection system is the optical lever [53, 111]. This method, depicted in Fig. 2.29, employs the same technique as light beam deflection galvanometers. A fairly well collimated light beam is reflected off a

Table 2.5 Noise in interferometers. F is the finesse of the cavity in the homodyne interferometer, P_i the incident power, P_d is the power on the detector, η is the sensitivity of the photodetector and RIN is the relative intensity noise of the laser. P_R and P_S are the power in the reference and sample beam in the heterodyne interferometer. P is the power in the Nomarski interferometer, $\delta\theta$ is the phase difference between the reference and the probe beam in the Nomarski interferometer. B is the bandwidth, e is the electron charge, λ is the wavelength of the laser, k the cantilever stiffness, ω_0 is the resonant frequency of the cantilever, Q is the quality factor of the cantilever, T is the temperature, and δi is the variation in current i

	Homodyne interferometer, fiber-optic interferometer	Heterodyne interferometer	Nomarski interferometer
Laser noise $\delta i^2{}_L$	$\frac{1}{4}\eta^2F^2P_i^2$ RIN	$\eta^2\left(P_R^2+P_S^2\right)$ RIN	$\frac{1}{16}\eta^2P^2\delta\theta$
Thermal noise $\delta i^2{}_T$	$\frac{16\pi^2}{\lambda^2}\eta^2F^2P_i^2\frac{4k_BTBQ}{\omega_0 k}$	$\frac{4\pi^2}{\lambda^2}\eta^2P_d^2\frac{4k_BTBQ}{\omega_0 k}$	$\frac{\pi^2}{\lambda^2}\eta^2P^2\frac{4k_BTBQ}{\omega_0 k}$
Shot noise $\delta i^2{}_S$	$4e\eta P_dB$	$2e\eta(P_R+P_S)B$	$\frac{1}{2}e\eta PB$

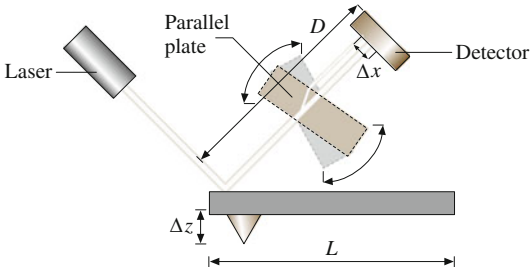

Fig. 2.29 Set-up for an optical lever detection microscope

mirror and projected to a receiving target. Any change in the angular position of the mirror will change the position where the light ray hits the target. Galvanometers use optical path lengths of several meters and scales projected onto the target wall are also used to monitor changes in position.

In an AFM using the optical lever method, a photodiode segmented into two (or four) closely spaced devices detects the orientation of the end of the cantilever. Initially, the light ray is set to hit the photodiodes in the middle of the two subdiodes. Any deflection of the cantilever will cause an imbalance of the number of photons reaching the two halves. Hence the electrical currents in the photodiodes will be unbalanced too. The difference signal is further amplified and is the input signal to the feedback loop. Unlike the interferometeric AFMs, where a modulation technique is often necessary to get a sufficient signal-to-noise ratio, most AFMs employing the optical lever method are operated in a static mode. AFMs based on the optical lever method are universally used. It is the simplest method for constructing an optical readout and it can be confined in volumes that are smaller than 5 cm in side length.

The optical lever detection system is a simple yet elegant way to detect normal and lateral force signals simultaneously [7, 8, 53, 111]. It has the additional advantage that it is a remote detection system.

Implementations

Light from a laser diode or from a super luminescent diode is focused on the end of the cantilever. The reflected light is directed onto a quadrant diode that measures the direction of the light beam. A Gaussian light beam far from its waist is characterized by an opening angle β. The deflection of the light beam by the cantilever surface tilted by an angle α is 2α. The intensity on the detector then shifts to the side by the product of 2α and the separation between the detector and the cantilever. The readout electronics calculates the difference in the photocurrents. The photocurrents, in turn, are proportional to the intensity incident on the diode.

The output signal is hence proportional to the change in intensity on the segments

$$I_{\text{sig}} \propto 4\frac{\alpha}{\beta} I_{\text{tot}}. \tag{2.47}$$

For the sake of simplicity, we assume that the light beam is of uniform intensity with its cross section increasing in proportion to the distance between the cantilever and the quadrant detector. The movement of the center of the light beam is then given by

$$\Delta x_{\text{Det}} = \Delta z \frac{D}{L}. \tag{2.48}$$

The photocurrent generated in a photodiode is proportional to the number of incoming photons hitting it. If the light beam contains a total number of N_0 photons, then the change in difference current becomes

$$\Delta(I_{\text{R}} - I_{\text{L}}) = \Delta I = \text{const}\ \Delta z\ D\ N_0. \tag{2.49}$$

Combining (2.48) and (2.49), one obtains that the difference current ΔI is independent of the separation of the quadrant detector and the cantilever. This relation is true if the light spot is smaller than the quadrant detector. If it is greater, the difference current ΔI becomes smaller with increasing distance. In reality, the light beam has a Gaussian intensity profile. For small movements Δx (compared to the diameter of the light spot at the quadrant detector), (2.49) still holds. Larger movements Δx, however, will introduce a nonlinear response. If the AFM is operated in a constant force mode, only small movements Δx of the light spot will occur. The feedback loop will cancel out all other movements.

The scanning of a sample with an AFM can twist the microfabricated cantilevers because of lateral forces [5, 7, 8] and affect the images [120]. When the tip is subjected to lateral forces, it will twist the cantilever and the light beam reflected from the end of the cantilever will be deflected perpendicular to the ordinary deflection direction. For many investigations this influence of lateral forces is unwanted. The design of the triangular cantilevers stems from the desire to minimize the torsion effects. However, lateral forces open up a new dimension in

force measurements. They allow, for instance, two materials to be distinguished because of their different friction coefficients, or adhesion energies to be determined. To measure lateral forces, the original optical lever AFM must be modified. The only modification compared with Fig. 2.29 is the use of a quadrant detector photodiode instead of a two-segment photodiode and the necessary readout electronics (Fig. 2.9a). The electronics calculates the following signals

$$\begin{aligned} U_{\text{normal force}} &= \alpha[(I_{\text{upper left}} + I_{\text{upper right}}) - (I_{\text{lower left}} + I_{\text{lower right}})], \\ U_{\text{lateral force}} &= \beta[(I_{\text{upper left}} + I_{\text{lower left}}) - (I_{\text{upper right}} + I_{\text{lower right}})]. \end{aligned} \tag{2.50}$$

The calculation of the lateral force as a function of the deflection angle does not have a simple solution for cross sections other than circles. An approximate formula for the angle of twist for rectangular beams is [151]

$$\theta = \frac{M_t L}{\beta G b^3 h}, \tag{2.51}$$

where $M_t = F_y \ell$ is the external twisting moment due to lateral force F_y and β a constant determined by the value of h/b. For the equation to hold, h has to be larger than b.

Inserting the values for a typical microfabricated cantilever with integrated tips

$$\begin{aligned} b &= 6 \times 10^{-7}\,\text{m}, \\ h &= 10^{-5}\,\text{m}, \\ L &= 10^{-4}\,\text{m}, \\ \ell &= 3.3 \times 10^{-6}\,\text{m}, \\ G &= 5 \times 10^{10}\,\text{Pa}, \\ \beta &= 0.333 \end{aligned} \tag{2.52}$$

into (2.51) we obtain the relation

$$F_y = 1.1 \times 10^{-4}\,\text{N} \times \theta. \tag{2.53}$$

Typical lateral forces are of the order of 10^{-10} N.

Sensitivity

The sensitivity of this set-up has been calculated in various papers [116, 148, 152]. Assuming a Gaussian beam, the resulting output signal as a function of the deflection angle is dispersion-like. Equation (2.47) shows that the sensitivity can be increased by increasing the intensity of the light beam I_{tot} or by decreasing the divergence of the laser beam. The upper bound of the intensity of the light I_{tot} is

given by saturation effects on the photodiode. If we decrease the divergence of a laser beam we automatically increase the beam waist. If the beam waist becomes larger than the width of the cantilever we start to get diffraction. Diffraction sets a lower bound on the divergence angle. Hence one can calculate the optimal beam waist w_{opt} and the optimal divergence angle β [148, 152]

$$\begin{aligned} w_{\text{opt}} &\approx 0.36b, \\ \theta_{\text{opt}} &\approx 0.89\frac{\lambda}{b}. \end{aligned} \tag{2.54}$$

The optimal sensitivity of the optical lever then becomes

$$\varepsilon[\text{mW/rad}] = 1.8\frac{b}{\lambda}I_{\text{tot}}[\text{mW}]. \tag{2.55}$$

The angular sensitivity of the optical lever can be measured by introducing a parallel plate into the beam. Tilting the parallel plate results in a displacement of the beam, mimicking an angular deflection.

Additional noise sources can be considered. Of little importance is the quantum mechanical uncertainty of the position [148, 152], which is, for typical cantilevers at room temperature

$$\Delta z = \sqrt{\frac{\hbar}{2m\omega_0}} = 0.05\,\text{fm}, \tag{2.56}$$

where $\hbar$ is the Planck constant ($=6.626\times10^{34}$ J s). At very low temperatures and for high-frequency cantilevers this could become the dominant noise source. A second noise source is the shot noise of the light. The shot noise is related to the particle number. We can calculate the number of photons incident on the detector using

$$n = \frac{I\tau}{\hbar\omega} = \frac{I\lambda}{2\pi B\hbar c} = 1.8\times10^9\frac{I[\text{W}]}{B[\text{Hz}]}, \tag{2.57}$$

where I is the intensity of the light, τ the measurement time, $B=1/\tau$ the bandwidth, and c the speed of light. The shot noise is proportional to the square root of the number of particles. Equating the shot noise signal with the signal resulting from the deflection of the cantilever one obtains

$$\Delta z_{\text{shot}} = 68\frac{L}{\omega}\sqrt{\frac{B[\text{kHz}]}{I[\text{mW}]}}[\text{fm}]. \tag{2.58}$$

where w is the diameter of the focal spot. Typical AFM set-ups have a shot noise of 2 pm. The thermal noise can be calculated from the equipartition principle. The amplitude at the resonant frequency is

$$\Delta z_{\text{therm}} = 129\sqrt{\frac{B}{k[\text{N/m}]\omega_0 Q}}\,[\text{pm}]. \tag{2.59}$$

A typical value is 16 pm. Upon touching the surface, the cantilever increases its resonant frequency by a factor of 4.39. This results in a new thermal noise amplitude of 3.2 pm for the cantilever in contact with the sample.

Piezoresistive Detection

Implementation

A piezoresistive cantilever is an alternative detection system which is not as widely used as the optical detection schemes [125, 126, 132]. This cantilever is based on the fact that the resistivities of certain materials, in particular Si, change with the applied stress. Figure 2.30 shows a typical implementation of a piezo-resistive cantilever. Four resistances are integrated on the chip, forming a Wheatstone bridge. Two of the resistors are in unstrained parts of the cantilever, and the other two measure the bending at the point of the maximal deflection. For instance, when an AC voltage is applied between terminals a and c, one can measure the detuning of the bridge between terminals b and d. With such a connection the output signal only varies due to bending, not due to changes in the ambient temperature and thus the coefficient of the piezoresistance.

Sensitivity

The resistance change is [126]

$$\frac{\Delta R}{R_0} = \Pi\delta. \tag{2.60}$$

where Π is the tensor element of the piezo-resistive coefficients, δ the mechanical stress tensor element and R_0 the equilibrium resistance. For a single resistor, they

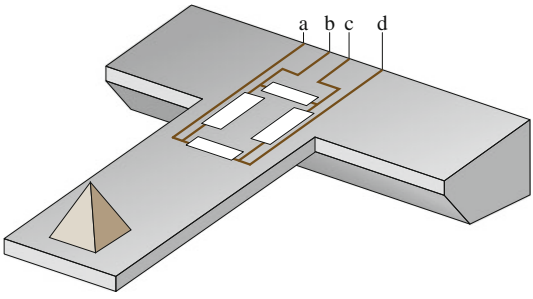

Fig. 2.30 A typical set-up for a piezoresistive readout

separate the mechanical stress and the tensor element into longitudinal and transverse components

$$\frac{\Delta R}{R_0} = \Pi_t \delta_t + \Pi_l \delta_l. \tag{2.61}$$

The maximum values of the stress components are $\Pi_t = 64.0 \times 10^{11}$ m^2/N and $\Pi_l = 71.4 \times 10^{11}$ m^2/N for a resistor oriented along the (110) direction in silicon [126]. In the resistor arrangement of Fig. 2.30, two of the resistors are subject to the longitudinal piezo-resistive effect and two of them are subject to the transversal piezo-resistive effect. The sensitivity of that set-up is about four times that of a single resistor, with the advantage that temperature effects cancel to first order. The resistance change is then calculated as

$$\frac{\Delta R}{R_0} = \Pi \frac{3Eh}{2L^2} \Delta z = \Pi \frac{6L}{bh^2} F_z, \tag{2.62}$$

where $\Pi = 67.7 \times 10^{11}$ m^2/N is the averaged piezo-resistive coefficient. Plugging in typical values for the dimensions (Fig. 2.24) ($L = 100$ µm, $b = 10$ µm, $h = 1$ µm), one obtains

$$\frac{\Delta R}{R_0} = \frac{4 \times 10^{-5}}{\text{nN}} F_z. \tag{2.63}$$

The sensitivity can be tailored by optimizing the dimensions of the cantilever.

Capacitance Detection

The capacitance of an arrangement of conductors depends on the geometry. Generally speaking, the capacitance increases for decreasing separations. Two parallel plates form a simple capacitor (Fig. 2.31, upper left), with capacitance

$$C = \frac{\varepsilon \varepsilon_0 A}{x}, \tag{2.64}$$

where A is the area of the plates, assumed equal, and x is the separation. Alternatively one can consider a sphere versus an infinite plane (Fig. 2.31, lower left). Here the capacitance is [116]

$$C = 4\pi\varepsilon_0 R \sum_{n=2}^{\infty} \frac{\sinh(\alpha)}{\sinh(n\alpha)} \tag{2.65}$$

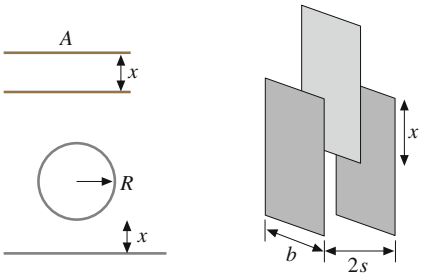

Fig. 2.31 Three possible arrangements of a capacitive readout. The *upper left* diagram shows a cross section through a parallel plate capacitor. The *lower left* diagram shows the geometry of a sphere versus a plane. The *right-hand* diagram shows the linear (but more complicated) capacitive readout

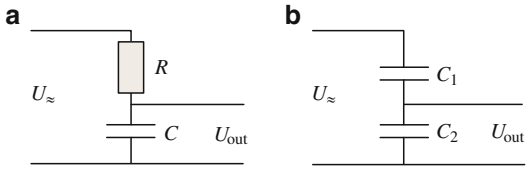

Fig. 2.32 Measuring the capacitance. **(a)** Low pass filter, **(b)** capacitive divider. C (*left*) and C_2 (*right*) are the capacitances under test

where R is the radius of the sphere, and α is defined by

$$\alpha = \ln\left(1 + \frac{z}{R} + \sqrt{\frac{z^2}{R^2} + 2\frac{z}{R}}\right). \tag{2.66}$$

One has to bear in mind that the capacitance of a parallel plate capacitor is a nonlinear function of the separation. One can circumvent this problem using a voltage divider. Figure 2.32a shows a low-pass filter. The output voltage is given by

$$\begin{aligned} U_{\text{out}} = U \approx \frac{\frac{1}{\mathrm{j}\omega C}}{R + \frac{1}{\mathrm{j}\omega C}} = U_{\approx}\frac{1}{\mathrm{j}\omega CR + 1} \\ \cong \frac{U_{\approx}}{\mathrm{j}\omega CR}. \end{aligned} \tag{2.67}$$

Here C is given by (2.64), ω is the excitation frequency and j is the imaginary unit. The approximate relation at the end is true when $\omega CR \gg 1$. This is equivalent to the statement that C is fed by a current source, since R must be large in this set-up. Plugging (2.64) into (2.67) and neglecting the phase information, one obtains

$$U_{\text{out}} = \frac{U_{\approx} x}{\omega R \varepsilon \varepsilon_0 A}, \tag{2.68}$$

which is linear in the displacement x.

Figure 2.32b shows a capacitive divider. Again the output voltage U_{out} is given by

$$U_{\text{out}} = U_{\approx}\frac{C_1}{C_2 + C_1} = U_{\approx}\frac{C_1}{\frac{\varepsilon\varepsilon_0 A}{x} + C_1}. \tag{2.69}$$

If there is a stray capacitance C_{s} then (2.69) is modified as

$$U_{\text{out}} = U_{\approx}\frac{C_1}{\frac{\varepsilon\varepsilon_0 A}{x} + C_{\text{s}} + C_1}. \tag{2.70}$$

Provided $C_{\text{s}} + C_1 \ll C_2$, one has a system which is linear in x. The driving voltage $U_{\approx}$ must be large (more than 100 V) to gave an output voltage in the range of 1 V. The linearity of the readout depends on the capacitance C_1 (Fig. 2.33).

Another idea is to keep the distance constant and to change the relative overlap of the plates (Fig. 2.31, right side). The capacitance of the moving center plate versus the stationary outer plates becomes

$$C = C_{\text{s}} + 2\frac{\varepsilon\varepsilon_0 bx}{s}, \tag{2.71}$$

where the variables are defined in Fig. 2.31. The stray capacitance comprises all effects, including the capacitance of the fringe fields. When the length x is comparable to the width b of the plates, one can safely assume that the stray capacitance is constant and independent of x. The main disadvantage of this set-up is that it is not as easily incorporated into a microfabricated device as the others.

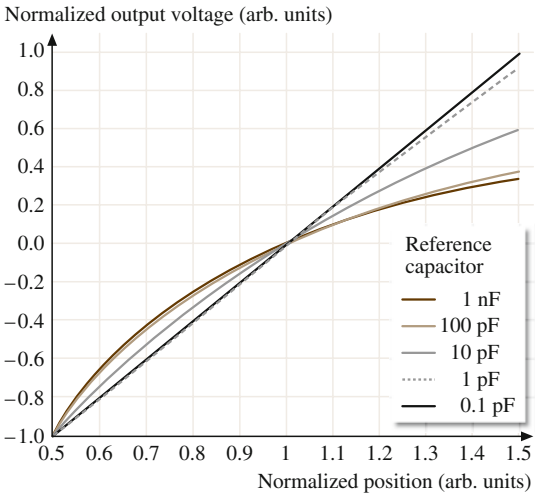

Fig. 2.33 Linearity of the capacitance readout as a function of the reference capacitor

Sensitivity

The capacitance itself is not a measure of the sensitivity, but its derivative is indicative of the signals one can expect. Using the situation described in Fig. 2.31 (upper left) and in (2.64), one obtains for the parallel plate capacitor

$$\frac{\mathrm{d}C}{\mathrm{d}x} = -\frac{\varepsilon\varepsilon_0 A}{x^2}. \tag{2.72}$$

Assuming a plate area A of 20 μm by 40 μm and a separation of 1 μm, one obtains a capacitance of 31 fF (neglecting stray capacitance and the capacitance of the connection leads) and a $\mathrm{d}C/\mathrm{d}x$ of 3.1×10^{-8} F/m =31 fF/μm. Hence it is of paramount importance to maximize the area between the two contacts and to minimize the distance x. The latter however is far from being trivial. One has to go to the limits of microfabrication to achieve a decent sensitivity.

If the capacitance is measured by the circuit shown in Fig. 2.32, one obtains for the sensitivity

$$\frac{\mathrm{d}U_{\mathrm{out}}}{U_{\approx}} = \frac{\mathrm{d}x}{\omega R\varepsilon\varepsilon_0 A}. \tag{2.73}$$

Using the same value for A as above, setting the reference frequency to 100 kHz, and selecting R =1 GΩ, we get the relative change in the output voltage U_{out} as

$$\frac{\mathrm{d}U_{\mathrm{out}}}{U_{\approx}} = \frac{22.5\times10^{-6}}{\text{Å}}\times\mathrm{d}x. \tag{2.74}$$

A driving voltage of 45 V then translates to a sensitivity of 1 mV/Å. A problem in this set-up is the stray capacitances. They are in parallel to the original capacitance and decrease the sensitivity considerably.

Alternatively, one could build an oscillator with this capacitance and measure the frequency. *RC*-oscillators typically have an oscillation frequency of

$$f_{\mathrm{res}} \propto \frac{1}{RC} = \frac{x}{R\varepsilon\varepsilon_0 A}. \tag{2.75}$$

Again the resistance R must be of the order of 1 GΩ when stray capacitances C_{s} are neglected. However C_{s} is of the order of 1 pF. Therefore one gets R =10 MΩ. Using these values, the sensitivity becomes

$$\mathrm{d}f_{\mathrm{res}} = \frac{C\ \mathrm{d}x}{R(C+C_{\mathrm{s}})^2 x} \approx \frac{0.1\ \mathrm{Hz}}{\text{Å}}\mathrm{d}x. \tag{2.76}$$

The bad thing is that the stray capacitances have made the signal nonlinear again. The linearized set-up in Fig. 2.31 has a sensitivity of

$$\frac{\mathrm{d}C}{\mathrm{d}x} = 2\frac{\varepsilon\varepsilon_0 b}{s}. \tag{2.77}$$

Substituting typical values (b =10 μm, s =1 μm), one gets dC/dx =1.8×10^{10} F/m. It is noteworthy that the sensitivity remains constant for scaled devices.

Implementations

Capacitance readout can be achieved in different ways [123, 124]. All include an alternating current or voltage with frequencies in the 100 kHz to 100 MHz range. One possibility is to build a tuned circuit with the capacitance of the cantilever determining the frequency. The resonance frequency of a high-quality Q tuned circuit is

$$\omega_0 = (LC)^{-1/2}. \tag{2.78}$$

where L is the inductance of the circuit. The capacitance C includes not only the sensor capacitance but also the capacitance of the leads. The precision of a frequency measurement is mainly determined by the ratio of L and C

$$Q = \left(\frac{L}{C}\right)^{1/2} \frac{1}{R}. \tag{2.79}$$

Here R symbolizes the losses in the circuit. The higher the quality, the more precise the frequency measurement. For instance, a frequency of 100 MHz and a capacitance of 1 pF gives an inductance of 250 μH. The quality then becomes 2.5×10^{8}. This value is an upper limit, since losses are usually too high.

Using a value of dC/dx =31 fF/μm, one gets ΔC/Å =3.1 aF/Å. With a capacitance of 1 pF, one gets

$$\begin{aligned} \frac{\Delta\omega}{\omega} &= \frac{1}{2}\frac{\Delta C}{C}, \\ \Delta\omega &= 100\,\mathrm{MHz} \times \frac{1}{2}\frac{3.1\mathrm{aF}}{1\,\mathrm{pF}} = 155\,\mathrm{Hz}. \end{aligned} \tag{2.80}$$

This is the frequency shift for a deflection of 1 Å. The calculation shows that this is a measurable quantity. The quality also indicates that there is no physical reason why this scheme should not work.

2.3.3 Combinations for 3-D Force Measurements

Three-dimensional force measurements are essential if one wants to know all of the details of the interaction between the tip and the cantilever. The straightforward attempt to measure three forces is complicated, since force sensors such as interferometers or capacitive sensors need a minimal detection volume, which is often too large. The second problem is that the force-sensing tip has to be held in some way. This implies that one of the three Cartesian axes is stiffer than the others.

However, by combining different sensors it is possible to achieve this goal. Straight cantilevers are employed for these measurements, because they can be handled analytically. The key observation is that the optical lever method does not determine the position of the end of the cantilever. It measures the orientation. In the previous sections, one has always made use of the fact that, for a force along one of the orthogonal symmetry directions at the end of the cantilever (normal force, lateral force, force along the cantilever beam axis), there is a one-to-one correspondence of the tilt angle and the deflection. The problem is that the force along the cantilever beam axis and the normal force create a deflection in the same direction. Hence, what is called the normal force component is actually a mixture of two forces. The deflection of the cantilever is the third quantity, which is not considered in most of the AFMs. A fiber-optic interferometer in parallel with the optical lever measures the deflection. Three measured quantities then allow the separation of the three orthonormal force directions, as is evident from (2.27) and (2.33) [12, 13, 14, 15, 16].

Alternatively, one can put the fast scanning direction along the axis of the cantilever. Forward and backward scans then exert opposite forces F_x. If the piezo movement is linearized, both force components in AFM based on optical lever detection can be determined. In this case, the normal force is simply the average of the forces in the forward and backward direction. The force F_x is the difference in the forces measured in the forward and backward directions.

2.3.4 Scanning and Control Systems

Almost all SPMs use piezo translators to scan the tip or the sample. Even the first STM [1, 103] and some of its predecessors [153, 154] used them. Other materials or set-ups for nanopositioning have been proposed, but they have not been successful [155, 156].

Piezo Tubes

A popular solution is tube scanners (Fig. 2.34). They are now widely used in SPMs due to their simplicity and their small size [133, 157]. The outer electrode is segmented into four equal sectors of 90°. Opposite sectors are driven by signals of the same magnitude, but opposite sign. This gives, through bending, two-dimensional movement on (approximately) a sphere. The inner electrode is normally driven by the z-signal. It is possible, however, to use only the outer electrodes for scanning and for the z-movement. The main drawback of applying the z-signal to the outer electrodes is that the applied voltage is the sum of both the x- or y-movements and the z-movement. Hence a larger scan size effectively reduces the available range for the z-control.

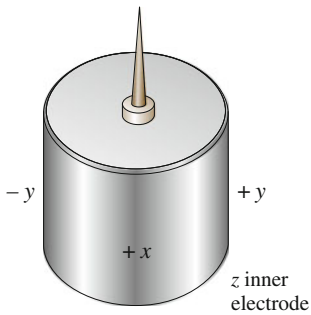

Fig. 2.34 Schematic drawing of a piezoelectric tube scanner. The piezo ceramic is molded into a tube form. The outer electrode is separated into four segments and connected to the scanning voltage. The z-voltage is applied to the inner electrode

Piezo Effect

An electric field applied across a piezoelectric material causes a change in the crystal structure, with expansion in some directions and contraction in others. Also, a net volume change occurs [132]. Many SPMs use the transverse piezo electric effect, where the applied electric field $\boldsymbol{E}$ is perpendicular to the expansion/contraction direction.

$$\Delta L = L(\boldsymbol{E} \cdot \boldsymbol{n}) d_{31} = L \frac{V}{t} d_{31}, \tag{2.81}$$

where d_{31} is the transverse piezoelectric constant, V is the applied voltage, t is the thickness of the piezo slab or the distance between the electrodes where the voltage is applied, L is the free length of the piezo slab, and $\boldsymbol{n}$ is the direction of polarization. Piezo translators based on the transverse piezoelectric effect have a wide range of sensitivities, limited mainly by mechanical stability and breakdown voltage.

Scan Range

The scanning range of a piezotube is difficult to calculate [157, 158, 159]. The bending of the tube depends on the electric fields and the nonuniform strain induced. A finite element calculation where the piezo tube was divided into 218 identical elements was used [158] to calculate the deflection. On each node, the mechanical stress, the stiffness, the strain and the piezoelectric stress were calculated when a voltage was applied on one electrode. The results were found to be linear on the first iteration and higher order corrections were very small even for large electrode voltages. It was found that, to first order, the x- and z-movement of the tube could be reasonably well approximated by assuming that the piezo tube is a segment of a torus. Using this model, one obtains

$$\mathrm{d}x = (V_+ - V_-)|d_{31}|\frac{L^2}{2td}, \tag{2.82}$$

$$\mathrm{d}z = (V_+ + V_- - 2V_z)|d_{31}|\frac{L}{2t}, \tag{2.83}$$

where $|d_{31}|$ is the coefficient of the transversal piezoelectric effect, L is the tube's free length, t is the tube's wall thickness, d is the tube's diameter, V_+ is the voltage on the positive outer electrode, while V is the voltage of the opposite quadrant negative electrode and V_z is the voltage of the inner electrode.

The cantilever or sample mounted on the piezotube has an additional lateral movement because the point of measurement is not in the endplane of the piezotube. The additional lateral displacement of the end of the tip is $\ell \sin\varphi \approx \ell\varphi$, where is the tip length and φ is the deflection angle of the end surface. Assuming that the sample or cantilever is always perpendicular to the end of the walls of the tube, and calculating with the torus model, one gets for the angle

$$\varphi = \frac{L}{R} = \frac{2dx}{L}, \tag{2.84}$$

where R is the radius of curvature of the piezo tube. Using the result of (2.84), one obtains for the additional x-movement

$$\mathrm{d}x_{\mathrm{add}} = \ell\varphi = \frac{2\mathrm{d}x\ell}{L} = (V_+ - V_-)|d_{31}|\frac{\ell L}{td} \tag{2.85}$$

and for the additional z-movement due to the x-movement

$$\mathrm{d}z_{\mathrm{add}} = \ell - \ell\cos\varphi = \frac{\ell\varphi^2}{2} = \frac{2\ell(\mathrm{d}x)^2}{L^2} = (V_+ - V_-)^2|d_{31}|^2\frac{\ell L^2}{2t^2d^2}. \tag{2.86}$$

Carr [158] assumed for his finite element calculations that the top of the tube was completely free to move and, as a consequence, the top surface was distorted, leading to a deflection angle that was about half that of the geometrical model. Depending on the attachment of the sample or the cantilever, this distortion may be smaller, leading to a deflection angle in-between that of the geometrical model and the one from the finite element calculation.

Nonlinearities and Creep

Piezo materials with a high conversion ratio (a large d_{31} or small electrode separations with large scanning ranges) are hampered by substantial hysteresis resulting in a deviation from linearity by more than 10%. The sensitivity of the piezo ceramic material (mechanical displacement divided by driving voltage) decreases with reduced scanning range, whereas the hysteresis is reduced. Careful selection of

the material used for the piezo scanners, the design of the scanners, and of the operating conditions is necessary to obtain optimum performance.

Passive Linearization: Calculation

The analysis of images affected by piezo nonlinearities [160, 161, 162, 163] shows that the dominant term is

$$x = AV + BV^2, \tag{2.87}$$

where x is the excursion of the piezo, V is the applied voltage and A and B are two coefficients describing the sensitivity of the material. Equation (2.87) holds for scanning from $V = 0$ to large V. For the reverse direction, the equation becomes

$$x = \tilde{A}V - \tilde{B}(V - V_{\max})^2, \tag{2.88}$$

where $\tilde{A}$ and $\tilde{B}$ are the coefficients for the back scan and $V_{\max}$ is the applied voltage at the turning point. Both equations demonstrate that the true x-travel is small at the beginning of the scan and becomes larger towards the end. Therefore, images are stretched at the beginning and compressed at the end.

Similar equations hold for the slow scan direction. The coefficients, however, are different. The combined action causes a greatly distorted image. This distortion can be calculated. The data acquisition systems record the signal as a function of V. However the data is measured as a function of x. Therefore we have to distribute the x-values evenly across the image. This can be done by inverting an approximation of (2.87). First we write

$$x = AV\left(1 - \frac{B}{A}V\right). \tag{2.89}$$

For $B \ll A$ we can approximate

$$V = \frac{x}{A}. \tag{2.90}$$

We now substitute (2.90) into the nonlinear term of (2.89). This gives

$$\begin{aligned} x &= AV\left(1 + \frac{Bx}{A^2}\right), \\ V &= \frac{x}{A}\,\frac{1}{(1 + Bx/A^2)} \approx \frac{x}{A}\left(1 - \frac{Bx}{A^2}\right). \end{aligned} \tag{2.91}$$

Hence an equation of the type

$$x_{\text{true}} = x(\alpha - \beta x/x_{\max}) \quad \text{with } 1 = \alpha - \beta \tag{2.92}$$

takes out the distortion of an image. α and β are dependent on the scan range, the scan speed and on the scan history, and have to be determined with exactly the same settings as for the measurement. $x_{\max}$ is the maximal scanning range. The condition for α and β guarantees that the image is transformed onto itself.

Similar equations to the empirical one shown above (2.92) can be derived by analyzing the movements of domain walls in piezo ceramics.

Passive Linearization: Measuring the Position

An alternative strategy is to measure the positions of the piezo translators. Several possibilities exist.

1. The interferometers described above can be used to measure the elongation of the piezo elongation. The fiber-optic interferometer is especially easy to implement. The coherence length of the laser only limits the measurement range. However, the signal is of a periodic nature. Hence direct use of the signal in a feedback circuit for the position is not possible. However, as a measurement tool and, especially, as a calibration tool, the interferometer is without competition. The wavelength of the light, for instance that in a He-Ne laser, is so well defined that the precision of the other components determines the error of the calibration or measurement.
2. The movement of the light spot on the quadrant detector can be used to measure the position of a piezo [164]. The output current changes by 0.5 A/cm $\times P$(W)/R (cm). Typical values (P =1 mW, R =0.001 cm) give 0.5 A/cm. The noise limit is typically $0.15\,\text{nm} \times \sqrt{\Delta f(\text{Hz})/H(\text{W/cm}^2)}$. Again this means that the laser beam above would have a 0.1 nm noise limitation for a bandwidth of 21 Hz. The advantage of this method is that, in principle, one can linearize two axes with only one detector.
3. A knife-edge blocking part of a light beam incident on a photodiode can be used to measure the position of the piezo. This technique, commonly used in optical shear force detection [75, 165], has a sensitivity of better than 0.1 nm.
4. The capacitive detection [166, 167] of the cantilever deflection can be applied to the measurement of the piezo elongation. Equations (2.64)–(2.79) apply to the problem. This technique is used in some commercial instruments. The difficulties lie in the avoidance of fringe effects at the borders of the two plates. While conceptually simple, one needs the latest technology in surface preparation to get a decent linearity. The electronic circuits used for the readout are often proprietary.
5. Linear variable differential transformers (LVDT) are a convenient way to measure positions down to 1 nm. They can be used together with a solid state joint set-up, as often used for large scan range stages. Unlike capacitive

detection, there are few difficulties in implementation. The sensors and the detection circuits LVDTs are available commercially.

6. A popular measurement technique is the use of strain gauges. They are especially sensitive when mounted on a solid state joint where the curvature is maximal. The resolution depends mainly on the induced curvature. A precision of 1 nm is attainable. The signals are low – a Wheatstone bridge is needed for the readout.

Active Linearization

Active linearization is done with feedback systems. Sensors need to be monotonic. Hence all of the systems described above, with the exception of the interferometers, are suitable. The most common solutions include the strain gauge approach, capacitance measurement or the LVDT, which are all electronic solutions. Optical detection systems have the disadvantage that the intensity enters into the calibration.

Alternative Scanning Systems

The first STMs were based on piezo tripods [1]. The piezo tripod (Fig. 2.35) is an intuitive way to generate the three-dimensional movement of a tip attached to its center. However, to get a suitable stability and scanning range, the tripod needs to be fairly large (about 50 mm). Some instruments use piezo stacks instead of monolithic piezoactuators. They are arranged in a tripod. Piezo stacks are thin layers of piezoactive materials glued together to form a device with up to 200 μm of actuation range. Preloading with a suitable metal casing reduces the nonlinearity.

If one tries to construct a homebuilt scanning system, the use of linearized scanning tables is recommended. They are built around solid state joints and actuated by piezo stacks. The joints guarantee that the movement is parallel with little deviation from the predefined scanning plane. Due to the construction it is easy to add measurement devices such as capacitive sensors, LVDTs or strain gauges, which are essential for a closed loop linearization. Two-dimensional tables

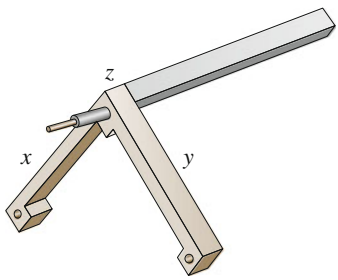

Fig. 2.35 An alternative type of piezo scanner: the tripod

can be bought from several manufacturers. They have linearities of better than 0.1% and a noise level of 10^{-4} – 10^{-5} for the maximal scanning range.

Control Systems

Basics

The electronics and software play an important role in the optimal performance of an SPM. Control electronics and software are supplied with commercial SPMs. Electronic control systems can use either analog or digital feedback. While digital feedback offers greater flexibility and ease of configuration, analog feedback circuits might be better suited for ultralow noise operation. We will describe here the basic set-ups for AFMs.

Figure 2.36 shows a block schematic of a typical AFM feedback loop. The signal from the force transducer is fed into the feedback loop, which consists mainly of a subtraction stage to get an error signal and an integrator. The gain of the integrator (high gain corresponds to short integration times) is set as high as possible without generating more than 1% overshoot. High gain minimizes the error margin of the current and forces the tip to follow the contours of constant density of states as well as possible. This operating mode is known as constant force mode. A high-voltage amplifier amplifies the outputs of the integrator. As AFMs using piezotubes usually require ±150 V at the output, the output of the integrator needs to be amplified by a high-voltage amplifier.

In order to scan the sample, additional voltages at high tension are required to drive the piezo. For example, with a tube scanner, four scanning voltages are required, namely $+V_x$, $-V_x$, $+V_y$ and $-V_y$. The x- and y-scanning voltages are generated in a scan generator (analog or computer-controlled). Both voltages are input to the two respective power amplifiers. Two inverting amplifiers generate the input voltages for the other two power amplifiers. The topography of the sample

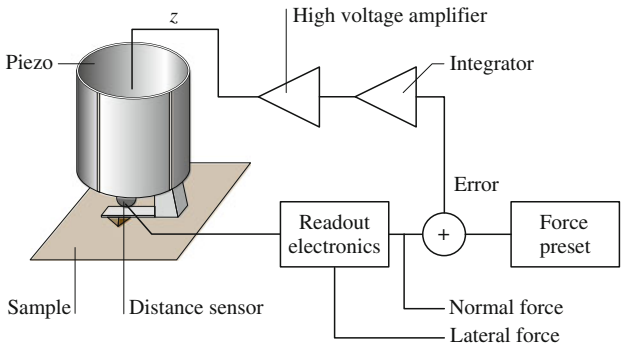

Fig. 2.36 Block schematic of the feedback control loop of an AFM

surface is determined by recording the input voltage to the high-voltage amplifier for the z-channel as a function of x and y (constant force mode).

Another operating mode is the variable force mode. The gain in the feedback loop is lowered and the scanning speed increased such that the force on the cantilever is no longer constant. Here the force is recorded as a function of x and y.

Force Spectroscopy

Four modes of spectroscopic imaging are in common use with force microscopes: measuring lateral forces, $\partial F/\partial z$, $\partial F/\partial x$ spatially resolved, and measuring force versus distance curves. Lateral forces can be measured by detecting the deflection of a cantilever in a direction orthogonal to the normal direction. The optical lever deflection method does this most easily. Lateral force measurements give indications of adhesion forces between the tip and the sample.

$\partial F/\partial z$ measurements probe the local elasticity of the sample surface. In many cases the measured quantity originates from a volume of a few cubic nanometers. The $\partial F/\partial z$ or local stiffness signal is proportional to Young's modulus, as far as one can define this quantity. Local stiffness is measured by vibrating the cantilever by a small amount in the z-direction. The expected signal for very stiff samples is zero: for very soft samples one also gets, independent of the stiffness, a constant signal. This signal is again zero for the optical lever deflection and equal to the driving amplitude for interferometric measurements. The best sensitivity is obtained when the compliance of the cantilever matches the stiffness of the sample.

A third spectroscopic quantity is the lateral stiffness. It is measured by applying a small modulation in the x-direction on the cantilever. The signal is again optimal when the lateral compliance of the cantilever matches the lateral stiffness of the sample. The lateral stiffness is, in turn, related to the shear modulus of the sample.

Detailed information on the interaction of the tip and the sample can be gained by measuring force versus distance curves. The cantilevers need to have enough compliance to avoid instabilities due to the attractive forces on the sample.

Using the Control Electronics as a Two-Dimensional Measurement Tool

Usually the control electronics of an AFM is used to control the x- and y-piezo signals while several data acquisition channels record the position-dependent signals. The control electronics can be used in another way: they can be viewed as a two-dimensional function generator. What is normally the x- and y-signal can be used to control two independent variables of an experiment. The control logic of the AFM then ensures that the available parameter space is systematically probed at equally spaced points. An example is friction force curves measured along a line across a step on graphite.

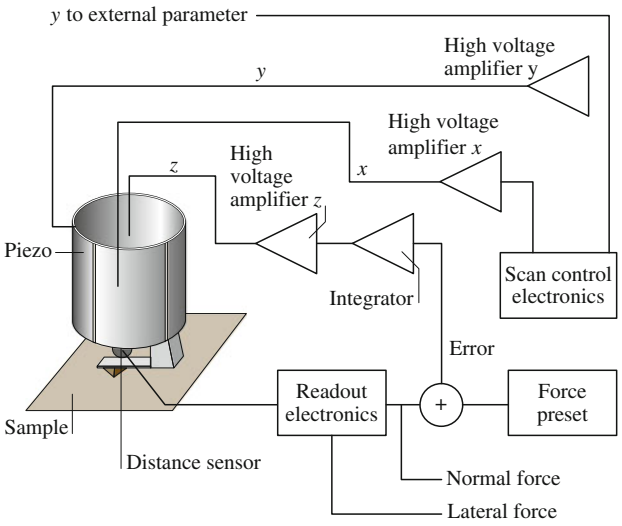

Fig. 2.37 Wiring of an AFM to measure friction force curves along a line

Figure 2.37 shows the connections. The *z*-piezo is connected as usual, like the *x*-piezo. However, the *y*-output is used to command the desired input parameter. The offset of the *y*-channel determines the position of the tip on the sample surface, together with the *x*-channel.

Some Imaging Processing Methods

The visualization and interpretation of images from AFMs is intimately connected to the processing of these images. An ideal AFM is a noise-free device that images a sample with perfect tips of known shape and has perfect linear scanning piezos. In reality, AFMs are not that ideal. The scanning device in an AFM is affected by distortions. The distortions are both linear and nonlinear. Linear distortions mainly result from imperfections in the machining of the piezotranslators causing crosstalk from the *z*-piezo to the *x*- and *y*-piezos, and vice versa. Among the linear distortions, there are two kinds which are very important. First, scanning piezos invariably have different sensitivities along the different scan axes due to variations in the piezo material and uneven electrode areas. Second, the same reasons might cause the scanning axes to be nonorthogonal. Furthermore, the plane in which the piezo-scanner moves for constant height *z* is hardly ever coincident with the sample plane. Hence, a linear ramp is added to the sample data. This ramp is especially bothersome when the height *z* is displayed as an intensity map.

The nonlinear distortions are harder to deal with. They can affect AFM data for a variety of reasons. First, piezoelectric ceramics do have a hysteresis loop, much like ferromagnetic materials. The deviations of piezoceramic materials from linearity

increase with increasing amplitude of the driving voltage. The mechanical position for one voltage depends on the previously applied voltages to the piezo. Hence, to get the best positional accuracy, one should always approach a point on the sample from the same direction. Another type of nonlinear distortion of images occurs when the scan frequency approaches the upper frequency limits of the *x*- and *y*-drive amplifiers or the upper frequency limit of the feedback loop (*z*-component). This distortion, due to the feedback loop, can only be minimized by reducing the scan frequency. On the other hand, there is a simple way to reduce distortions due to the *x*- and *y*-piezo drive amplifiers. To keep the system as simple as possible, one normally uses a triangular waveform to drive the scanning piezos. However, triangular waves contain frequency components as multiples of the scan frequency. If the cut-off frequencies of the *x*- and *y*-drive electronics or of the feedback loop are too close to the scanning frequency (two or three times the scanning frequency), the triangular drive voltage is rounded off at the turning points. This rounding error causes, first, a distortion of the scan linearity and, second, through phase lags, the projection of part of the backward scan onto the forward scan. This type of distortion can be minimized by carefully selecting the scanning frequency and by using driving voltages for the *x*- and *y*-piezos with waveforms like trapezoidal waves, which are closer to a sine wave. The values measured for *x*-, *y*- or *z*-piezos are affected by noise. The origin of this noise can be either electronic, disturbances, or a property of the sample surface due to adsorbates. In addition to this incoherent noise, interference with main and other equipment nearby might be present. Depending on the type of noise, one can filter it in real space or in Fourier space. The most important part of image processing is to visualize the measured data. Typical AFM data sets can consist of many thousands to over a million points per plane. There may be more than one image plane present. The AFM data represents a topography in various data spaces.

Most commercial data acquisition systems implicitly use some kind of data processing. Since the original data is commonly subject to slopes on the surface, most programs use some kind of slope correction. The least disturbing way is to subtract a plane $z(x, y) = Ax + By + C$ from the data. The coefficients are determined by fitting $z(x, y)$ to the data. Another operation is to subtract a second-order function such as $z(x, y) = Ax^2 + By^2 + Cxy + Dx + Ey + F$. Again, the parameters are determined with a fit. This function is appropriate for almost planar data, where the nonlinearity of the piezos caused the distortion.

In the image processing software from Digital Instruments, up to three operations are performed on the raw data. First, a zero-order flatten is applied. The flatten operation is used to eliminate image bow in the slow scan direction (caused by a physical bow in the instrument itself), slope in the slow scan direction, and bands in the image (caused by differences in the scan height from one scan line to the next). The flattening operation takes each scan line and subtracts the average value of the height along each scan line from each point in that scan line. This brings each scan line to the same height. Next, a first-order plane fit is applied in the fast scan direction. The plane-fit operation is used to eliminate bow and slope in the fast scan direction. The plane fit operation calculates a best fit plane for the image and

subtracts it from the image. This plane has a constant nonzero slope in the fast scan direction. In some cases a higher order polynomial *plane* may be required. Depending upon the quality of the raw data, the flattening operation and/or the plane fit operation may not be required at all.

References

1. G. Binnig, H. Rohrer, C. Gerber, E. Weibel, Surface studies by scanning tunneling microscopy, Phys. Rev. Lett. **49**, 57–61 (1982)
2. G. Binnig, C.F. Quate, C. Gerber, Atomic force microscope, Phys. Rev. Lett. **56**, 930–933 (1986)
3. G. Binnig, C. Gerber, E. Stoll, T.R. Albrecht, C.F. Quate, Atomic resolution with atomic force microscope, Europhys. Lett. **3**, 1281–1286 (1987)
4. B. Bhushan, *Handbook of Micro-/Nanotribology*, 2nd edn. (CRC, Boca Raton 1999)
5. C.M. Mate, G.M. McClelland, R. Erlandsson, S. Chiang, Atomic-scale friction of a tungsten tip on a graphite surface, Phys. Rev. Lett. **59**, 1942–1945 (1987)
6. R. Erlandsson, G.M. McClelland, C.M. Mate, S. Chiang, Atomic force microscopy using optical interferometry, J. Vac. Sci. Technol. A **6**, 266–270 (1988)
7. O. Marti, J. Colchero, J. Mlynek, Combined scanning force and friction microscopy of mica, Nanotechnology **1**, 141–144 (1990)
8. G. Meyer, N.M. Amer, Simultaneous measurement of lateral and normal forces with an optical-beam-deflection atomic force microscope, Appl. Phys. Lett. **57**, 2089–2091 (1990)
9. B. Bhushan, J. Ruan, Atomic-scale friction measurements using friction force microscopy: Part II – Application to magnetic media, ASME J. Tribol. **116**, 389–396 (1994)
10. B. Bhushan, V.N. Koinkar, J. Ruan, Microtribology of magnetic media, Proc. Inst. Mech. Eng. Part J **208**, 17–29 (1994)
11. B. Bhushan, J.N. Israelachvili, U. Landman, Nanotribology: Friction, wear, and lubrication at the atomic scale, Nature **374**, 607–616 (1995)
12. S. Fujisawa, M. Ohta, T. Konishi, Y. Sugawara, S. Morita, Difference between the forces measured by an optical lever deflection and by an optical interferometer in an atomic force microscope, Rev. Sci. Instrum. **65**, 644–647 (1994)
13. S. Fujisawa, E. Kishi, Y. Sugawara, S. Morita, Fluctuation in 2-dimensional stick-slip phenomenon observed with 2-dimensional frictional force microscope, Jpn. J. Appl. Phys. **33**, 3752–3755 (1994)
14. S. Grafstrom, J. Ackermann, T. Hagen, R. Neumann, O. Probst, Analysis of lateral force effects on the topography in scanning force microscopy, J. Vac. Sci. Technol. B **12**, 1559–1564 (1994)
15. R.M. Overney, H. Takano, M. Fujihira, W. Paulus, H. Ringsdorf, Anisotropy in friction and molecular stick-slip motion, Phys. Rev. Lett. **72**, 3546–3549 (1994)
16. R.J. Warmack, X.Y. Zheng, T. Thundat, D.P. Allison, Friction effects in the deflection of atomic force microscope cantilevers, Rev. Sci. Instrum. **65**, 394–399 (1994)
17. N.A. Burnham, D.D. Domiguez, R.L. Mowery, R.J. Colton, Probing the surface forces of monolayer films with an atomic force microscope, Phys. Rev. Lett. **64**, 1931–1934 (1990)
18. N.A. Burham, R.J. Colton, H.M. Pollock, Interpretation issues in force microscopy, J. Vac. Sci. Technol. A **9**, 2548–2556 (1991)
19. C.D. Frisbie, L.F. Rozsnyai, A. Noy, M.S. Wrighton, C.M. Lieber, Functional group imaging by chemical force microscopy, Science **265**, 2071–2074 (1994)
20. V.N. Koinkar, B. Bhushan, Microtribological studies of unlubricated and lubricated surfaces using atomic force/friction force microscopy, J. Vac. Sci. Technol. A **14**, 2378–2391 (1996)

21. V. Scherer, B. Bhushan, U. Rabe, W. Arnold, Local elasticity and lubrication measurements using atomic force and friction force microscopy at ultrasonic frequencies, IEEE Trans. Magn. **33**, 4077–4079 (1997)
22. V. Scherer, W. Arnold, B. Bhushan, Lateral force microscopy using acoustic friction force microscopy, Surf. Interface Anal. **27**, 578–587 (1999)
23. B. Bhushan, S. Sundararajan, Micro-/nanoscale friction and wear mechanisms of thin films using atomic force and friction force microscopy, Acta Mater. **46**, 3793–3804 (1998)
24. U. Krotil, T. Stifter, H. Waschipky, K. Weishaupt, S. Hild, O. Marti, Pulse force mode: A new method for the investigation of surface properties, Surf. Interface Anal. **27**, 336–340 (1999)
25. B. Bhushan, C. Dandavate, Thin-film friction and adhesion studies using atomic force microscopy, J. Appl. Phys. **87**, 1201–1210 (2000)
26. B. Bhushan, *Micro-/Nanotribology and Its Applications* (Kluwer, Dordrecht 1997)
27. B. Bhushan, *Principles and Applications of Tribology* (Wiley, New York 1999)
28. B. Bhushan, *Modern Tribology Handbook – Vol. 1: Principles of Tribology* (CRC, Boca Raton 2001)
29. B. Bhushan, *Introduction to Tribology* (Wiley, New York 2002)
30. M. Reinstädtler, U. Rabe, V. Scherer, U. Hartmann, A. Goldade, B. Bhushan, W. Arnold, On the nanoscale measurement of friction using atomic force microscope cantilever torsional resonances, Appl. Phys. Lett. **82**, 2604–2606 (2003)
31. N.A. Burnham, R.J. Colton, Measuring the nanomechanical properties and surface forces of materials using an atomic force microscope, J. Vac. Sci. Technol. A **7**, 2906–2913 (1989)
32. P. Maivald, H.J. Butt, S.A.C. Gould, C.B. Prater, B. Drake, J.A. Gurley, V.B. Elings, P.K. Hansma, Using force modulation to image surface elasticities with the atomic force microscope, Nanotechnology **2**, 103–106 (1991)
33. B. Bhushan, A.V. Kulkarni, W. Bonin, J.T. Wyrobek, Nano/picoindentation measurements using capacitive transducer in atomic force microscopy, Philos. Mag. A **74**, 1117–1128 (1996)
34. B. Bhushan, V.N. Koinkar, Nanoindentation hardness measurements using atomic force microscopy, Appl. Phys. Lett. **75**, 5741–5746 (1994)
35. D. DeVecchio, B. Bhushan, Localized surface elasticity measurements using an atomic force microscope, Rev. Sci. Instrum. **68**, 4498–4505 (1997)
36. S. Amelio, A.V. Goldade, U. Rabe, V. Scherer, B. Bhushan, W. Arnold, Measurements of mechanical properties of ultra-thin diamond-like carbon coatings using atomic force acoustic microscopy, Thin Solid Films **392**, 75–84 (2001)
37. D.M. Eigler, E.K. Schweizer, Positioning single atoms with a scanning tunnelling microscope, Nature **344**, 524–528 (1990)
38. A.L. Weisenhorn, J.E. MacDougall, J.A.C. Gould, S.D. Cox, W.S. Wise, J. Massie, P. Maivald, V.B. Elings, G.D. Stucky, P.K. Hansma, Imaging and manipulating of molecules on a zeolite surface with an atomic force microscope, Science **247**, 1330–1333 (1990)
39. I.W. Lyo, P. Avouris, Field-induced nanometer-to-atomic-scale manipulation of silicon surfaces with the STM, Science **253**, 173–176 (1991)
40. O.M. Leung, M.C. Goh, Orientation ordering of polymers by atomic force microscope tip-surface interactions, Science **225**, 64–66 (1992)
41. D.W. Abraham, H.J. Mamin, E. Ganz, J. Clark, Surface modification with the scanning tunneling microscope, IBM J. Res. Dev. **30**, 492–499 (1986)
42. R.M. Silver, E.E. Ehrichs, A.L. de Lozanne, Direct writing of submicron metallic features with a scanning tunnelling microscope, Appl. Phys. Lett. **51**, 247–249 (1987)
43. A. Kobayashi, F. Grey, R.S. Williams, M. Ano, Formation of nanometer-scale grooves in silicon with a scanning tunneling microscope, Science **259**, 1724–1726 (1993)
44. B. Parkinson, Layer-by-layer nanometer scale etching of two-dimensional substrates using the scanning tunneling microscopy, J. Am. Chem. Soc. **112**, 7498–7502 (1990)

45. A. Majumdar, P.I. Oden, J.P. Carrejo, L.A. Nagahara, J.J. Graham, J. Alexander, Nanometer-scale lithography using the atomic force microscope, Appl. Phys. Lett. **61**, 2293–2295 (1992)
46. B. Bhushan, Micro-/nanotribology and its applications to magnetic storage devices and MEMS, Tribol. Int. **28**, 85–96 (1995)
47. L. Tsau, D. Wang, K.L. Wang, Nanometer scale patterning of silicon(100) surface by an atomic force microscope operating in air, Appl. Phys. Lett. **64**, 2133–2135 (1994)
48. E. Delawski, B.A. Parkinson, Layer-by-layer etching of two-dimensional metal chalcogenides with the atomic force microscope, J. Am. Chem. Soc. **114**, 1661–1667 (1992)
49. B. Bhushan, G.S. Blackman, Atomic force microscopy of magnetic rigid disks and sliders and its applications to tribology, ASME J. Tribol. **113**, 452–458 (1991)
50. O. Marti, B. Drake, P.K. Hansma, Atomic force microscopy of liquid-covered surfaces: atomic resolution images, Appl. Phys. Lett. **51**, 484–486 (1987)
51. B. Drake, C.B. Prater, A.L. Weisenhorn, S.A.C. Gould, T.R. Albrecht, C.F. Quate, D.S. Cannell, H.G. Hansma, P.K. Hansma, Imaging crystals, polymers and processes in water with the atomic force microscope, Science **243**, 1586–1589 (1989)
52. M. Binggeli, R. Christoph, H.E. Hintermann, J. Colchero, O. Marti, Friction force measurements on potential controlled graphite in an electrolytic environment, Nanotechnology **4**, 59–63 (1993)
53. G. Meyer, N.M. Amer, Novel optical approach to atomic force microscopy, Appl. Phys. Lett. **53**, 1045–1047 (1988)
54. J.H. Coombs, J.B. Pethica, Properties of vacuum tunneling currents: Anomalous barrier heights, IBM J. Res. Dev. **30**, 455–459 (1986)
55. M.D. Kirk, T. Albrecht, C.F. Quate, Low-temperature atomic force microscopy, Rev. Sci. Instrum. **59**, 833–835 (1988)
56. F.J. Giessibl, C. Gerber, G. Binnig, A low-temperature atomic force/scanning tunneling microscope for ultrahigh vacuum, J. Vac. Sci. Technol. B **9**, 984–988 (1991)
57. T.R. Albrecht, P. Grutter, D. Rugar, D.P.E. Smith, Low temperature force microscope with all-fiber interferometer, Ultramicroscopy **42–44**, 1638–1646 (1992)
58. H.J. Hug, A. Moser, T. Jung, O. Fritz, A. Wadas, I. Parashikor, H.J. Güntherodt, Low temperature magnetic force microscopy, Rev. Sci. Instrum. **64**, 2920–2925 (1993)
59. C. Basire, D.A. Ivanov, Evolution of the lamellar structure during crystallization of a semicrystalline-amorphous polymer blend: Time-resolved hot-stage SPM study, Phys. Rev. Lett. **85**, 5587–5590 (2000)
60. H. Liu, B. Bhushan, Investigation of nanotribological properties of self-assembled monolayers with alkyl and biphenyl spacer chains, Ultramicroscopy **91**, 185–202 (2002)
61. J. Foster, J. Frommer, Imaging of liquid crystal using a tunneling microscope, Nature **333**, 542–547 (1988)
62. D. Smith, H. Horber, C. Gerber, G. Binnig, Smectic liquid crystal monolayers on graphite observed by scanning tunneling microscopy, Science **245**, 43–45 (1989)
63. D. Smith, J. Horber, G. Binnig, H. Nejoh, Structure, registry and imaging mechanism of alkylcyanobiphenyl molecules by tunnelling microscopy, Nature **344**, 641–644 (1990)
64. Y. Andoh, S. Oguchi, R. Kaneko, T. Miyamoto, Evaluation of very thin lubricant films, J. Phys. D **25**, A71–A75 (1992)
65. Y. Martin, C.C. Williams, H.K. Wickramasinghe, Atomic force microscope-force mapping and profiling on a sub 100Åscale, J. Appl. Phys. **61**, 4723–4729 (1987)
66. J.E. Stern, B.D. Terris, H.J. Mamin, D. Rugar, Deposition and imaging of localized charge on insulator surfaces using a force microscope, Appl. Phys. Lett. **53**, 2717–2719 (1988)
67. K. Yamanaka, H. Ogisco, O. Kolosov, Ultrasonic force microscopy for nanometer resolution subsurface imaging, Appl. Phys. Lett. **64**, 178–180 (1994)
68. K. Yamanaka, E. Tomita, Lateral force modulation atomic force microscope for selective imaging of friction forces, Jpn. J. Appl. Phys. **34**, 2879–2882 (1995)
69. U. Rabe, K. Janser, W. Arnold, Vibrations of free and surface-coupled atomic force microscope: Theory and experiment, Rev. Sci. Instrum. **67**, 3281–3293 (1996)

70. Y. Martin, H.K. Wickramasinghe, Magnetic imaging by force microscopy with 1000Å resolution, Appl. Phys. Lett. **50**, 1455–1457 (1987)
71. D. Rugar, H.J. Mamin, P. Güthner, S.E. Lambert, J.E. Stern, I. McFadyen, T. Yogi, Magnetic force microscopy – General principles and application to longitudinal recording media, J. Appl. Phys. **63**, 1169–1183 (1990)
72. C. Schönenberger, S.F. Alvarado, Understanding magnetic force microscopy, Z. Phys. B **80**, 373–383 (1990)
73. U. Hartmann, Magnetic force microscopy, Annu. Rev. Mater. Sci. **29**, 53–87 (1999)
74. D.W. Pohl, W. Denk, M. Lanz, Optical stethoscopy-image recording with resolution lambda/20, Appl. Phys. Lett. **44**, 651–653 (1984)
75. E. Betzig, J.K. Troutman, T.D. Harris, J.S. Weiner, R.L. Kostelak, Breaking the diffraction barrier – optical microscopy on a nanometric scale, Science **251**, 1468–1470 (1991)
76. E. Betzig, P.L. Finn, J.S. Weiner, Combined shear force and near-field scanning optical microscopy, Appl. Phys. Lett. **60**, 2484 (1992)
77. P.F. Barbara, D.M. Adams, D.B. O'Connor, Characterization of organic thin film materials with near-field scanning optical microscopy (NSOM), Annu. Rev. Mater. Sci. **29**, 433–469 (1999)
78. C.C. Williams, H.K. Wickramasinghe, Scanning thermal profiler, Appl. Phys. Lett. **49**, 1587–1589 (1986)
79. C.C. Williams, H.K. Wickramasinghe, Microscopy of chemical-potential variations on an atomic scale, Nature **344**, 317–319 (1990)
80. A. Majumdar, Scanning thermal microscopy, Annu. Rev. Mater. Sci. **29**, 505–585 (1999)
81. O.E. Husser, D.H. Craston, A.J. Bard, Scanning electrochemical microscopy – High resolution deposition and etching of materials, J. Electrochem. Soc. **136**, 3222–3229 (1989)
82. Y. Martin, D.W. Abraham, H.K. Wickramasinghe, High-resolution capacitance measurement and potentiometry by force microscopy, Appl. Phys. Lett. **52**, 1103–1105 (1988)
83. M. Nonnenmacher, M.P. O'Boyle, H.K. Wickramasinghe, Kelvin probe force microscopy, Appl. Phys. Lett. **58**, 2921–2923 (1991)
84. J.M.R. Weaver, D.W. Abraham, High resolution atomic force microscopy potentiometry, J. Vac. Sci. Technol. B **9**, 1559–1561 (1991)
85. D. DeVecchio, B. Bhushan, Use of a nanoscale Kelvin probe for detecting wear precursors, Rev. Sci. Instrum. **69**, 3618–3624 (1998)
86. B. Bhushan, A.V. Goldade: Measurements and analysis of surface potential change during wear of single-crystal silicon (100) at ultralow loads using Kelvin probe microscopy, Appl. Surf. Sci. **157**, 373–381 (2000)
87. P.K. Hansma, B. Drake, O. Marti, S.A.C. Gould, C.B. Prater, The scanning ion-conductance microscope, Science **243**, 641–643 (1989)
88. C.B. Prater, P.K. Hansma, M. Tortonese, C.F. Quate, Improved scanning ion-conductance microscope using microfabricated probes, Rev. Sci. Instrum. **62**, 2634–2638 (1991)
89. J. Matey, J. Blanc, Scanning capacitance microscopy, J. Appl. Phys. **57**, 1437–1444 (1985)
90. C.C. Williams, Two-dimensional dopant profiling by scanning capacitance microscopy, Annu. Rev. Mater. Sci. **29**, 471–504 (1999)
91. D.T. Lee, J.P. Pelz, B. Bhushan, Instrumentation for direct, low frequency scanning capacitance microscopy, and analysis of position dependent stray capacitance, Rev. Sci. Instrum. **73**, 3523–3533 (2002)
92. P.K. Hansma, J. Tersoff, Scanning tunneling microscopy, J. Appl. Phys. **61**, R1–R23 (1987)
93. I. Giaever, Energy gap in superconductors measured by electron tunneling, Phys. Rev. Lett. **5**, 147–148 (1960)
94. D. Sarid, V. Elings, Review of scanning force microscopy, J. Vac. Sci. Technol. B **9**, 431–437 (1991)
95. U. Durig, O. Zuger, A. Stalder, Interaction force detection in scanning probe microscopy: Methods and applications, J. Appl. Phys. **72**, 1778–1797 (1992)

96. J. Frommer, Scanning tunneling microscopy and atomic force microscopy in organic chemistry, Angew. Chem. Int. Ed. **31**, 1298–1328 (1992)
97. H.J. Güntherodt, R. Wiesendanger (Eds.), *Scanning Tunneling Microscopy I: General Principles and Applications to Clean and Adsorbate-Covered Surfaces* (Springer, Berlin, Heidelberg 1992)
98. R. Wiesendanger, H.J. Güntherodt (Eds.), *Scanning Tunneling Microscopy II: Further Applications and Related Scanning Techniques* (Springer, Berlin, Heidelberg 1992)
99. D.A. Bonnell (Ed.), *Scanning Tunneling Microscopy and Spectroscopy – Theory, Techniques, and Applications* (VCH, New York 1993)
100. O. Marti, M. Amrein (Eds.), *STM and SFM in Biology* (Academic, San Diego 1993)
101. J.A. Stroscio, W.J. Kaiser (Eds.), *Scanning Tunneling Microscopy* (Academic, Boston 1993)
102. H.J. Güntherodt, D. Anselmetti, E. Meyer (Eds.), *Forces in Scanning Probe Methods* (Kluwer, Dordrecht 1995)
103. G. Binnig, H. Rohrer, Scanning tunnelling microscopy, Surf. Sci. **126**, 236–244 (1983)
104. B. Bhushan, J. Ruan, B.K. Gupta, A scanning tunnelling microscopy study of fullerene films, J. Phys. D **26**, 1319–1322 (1993)
105. R.L. Nicolaides, W.E. Yong, W.F. Packard, H.A. Zhou, Scanning tunneling microscope tip structures, J. Vac. Sci. Technol. A **6**, 445–447 (1988)
106. J.P. Ibe, P.P. Bey, S.L. Brandon, R.A. Brizzolara, N.A. Burnham, D.P. DiLella, K.P. Lee, C.R.K. Marrian, R.J. Colton, On the electrochemical etching of tips for scanning tunneling microscopy, J. Vac. Sci. Technol. A **8**, 3570–3575 (1990)
107. R. Kaneko, S. Oguchi, Ion-implanted diamond tip for a scanning tunneling microscope, Jpn. J. Appl. Phys. **28**, 1854–1855 (1990)
108. F.J. Giessibl, Atomic resolution of the silicon(111)–(7×7) surface by atomic force microscopy, Science **267**, 68–71 (1995)
109. B. Anczykowski, D. Krüger, K.L. Babcock, H. Fuchs, Basic properties of dynamic force spectroscopy with the scanning force microscope in experiment and simulation, Ultramicroscopy **66**, 251–259 (1996)
110. T.R. Albrecht, C.F. Quate, Atomic resolution imaging of a nonconductor by atomic force microscopy, J. Appl. Phys. **62**, 2599–2602 (1987)
111. S. Alexander, L. Hellemans, O. Marti, J. Schneir, V. Elings, P.K. Hansma, An atomic-resolution atomic-force microscope implemented using an optical lever, J. Appl. Phys. **65**, 164–167 (1989)
112. G. Meyer, N.M. Amer, Optical-beam-deflection atomic force microscopy: The NaCl(001) surface, Appl. Phys. Lett. **56**, 2100–2101 (1990)
113. A.L. Weisenhorn, M. Egger, F. Ohnesorge, S.A.C. Gould, S.P. Heyn, H.G. Hansma, R.L. Sinsheimer, H.E. Gaub, P.K. Hansma, Molecular resolution images of Langmuir–Blodgett films and DNA by atomic force microscopy, Langmuir **7**, 8–12 (1991)
114. J. Ruan, B. Bhushan, Atomic-scale and microscale friction of graphite and diamond using friction force microscopy, J. Appl. Phys. **76**, 5022–5035 (1994)
115. D. Rugar, P.K. Hansma, Atomic force microscopy, Phys. Today **43**, 23–30 (1990)
116. D. Sarid, *Scanning Force Microscopy* (Oxford Univ. Press, Oxford 1991)
117. G. Binnig, Force microscopy, Ultramicroscopy **42–44**, 7–15 (1992)
118. E. Meyer, Atomic force microscopy, Surf. Sci. **41**, 3–49 (1992)
119. H.K. Wickramasinghe, Progress in scanning probe microscopy, Acta Mater. **48**, 347–358 (2000)
120. A.J. den Boef, The influence of lateral forces in scanning force microscopy, Rev. Sci. Instrum. **62**, 88–92 (1991)
121. M. Radmacher, R.W. Tillman, M. Fritz, H.E. Gaub, From molecules to cells: Imaging soft samples with the atomic force microscope, Science **257**, 1900–1905 (1992)
122. F. Ohnesorge, G. Binnig, True atomic resolution by atomic force microscopy through repulsive and attractive forces, Science **260**, 1451–1456 (1993)

123. G. Neubauer, S.R. Coben, G.M. McClelland, D. Horne, C.M. Mate, Force microscopy with a bidirectional capacitance sensor, Rev. Sci. Instrum. **61**, 2296–2308 (1990)
124. T. Goddenhenrich, H. Lemke, U. Hartmann, C. Heiden, Force microscope with capacitive displacement detection, J. Vac. Sci. Technol. A **8**, 383–387 (1990)
125. U. Stahl, C.W. Yuan, A.L. Delozanne, M. Tortonese, Atomic force microscope using piezoresistive cantilevers and combined with a scanning electron microscope, Appl. Phys. Lett. **65**, 2878–2880 (1994)
126. R. Kassing, E. Oesterschulze, Sensors for scanning probe microscopy. In: *Micro-/Nanotribology and Its Applications*, ed. by B. Bhushan (Kluwer, Dordrecht 1997) pp.35–54
127. C.M. Mate, Atomic-force-microscope study of polymer lubricants on silicon surfaces, Phys. Rev. Lett. **68**, 3323–3326 (1992)
128. S.P. Jarvis, A. Oral, T.P. Weihs, J.B. Pethica, A novel force microscope and point contact probe, Rev. Sci. Instrum. **64**, 3515–3520 (1993)
129. D. Rugar, H.J. Mamin, P. Güthner, Improved fiber-optical interferometer for atomic force microscopy, Appl. Phys. Lett. **55**, 2588–2590 (1989)
130. C. Schönenberger, S.F. Alvarado, A differential interferometer for force microscopy, Rev. Sci. Instrum. **60**, 3131–3135 (1989)
131. D. Sarid, D. Iams, V. Weissenberger, L.S. Bell, Compact scanning-force microscope using laser diode, Opt. Lett. **13**, 1057–1059 (1988)
132. N.W. Ashcroft, N.D. Mermin, *Solid State Physics* (Holt Reinhart and Winston, New York 1976)
133. G. Binnig, D.P.E. Smith, Single-tube three-dimensional scanner for scanning tunneling microscopy, Rev. Sci. Instrum. **57**, 1688 (1986)
134. S.I. Park, C.F. Quate, Digital filtering of STM images, J. Appl. Phys. **62**, 312 (1987)
135. J.W. Cooley, J.W. Tukey, An algorithm for machine calculation of complex Fourier series, Math. Comput. **19**, 297 (1965)
136. J. Ruan, B. Bhushan, Atomic-scale friction measurements using friction force microscopy: Part I – General principles and new measurement techniques, ASME J. Tribol. **116**, 378–388 (1994)
137. T.R. Albrecht, S. Akamine, T.E. Carver, C.F. Quate, Microfabrication of cantilever styli for the atomic force microscope, J. Vac. Sci. Technol. A **8**, 3386–3396 (1990)
138. O. Marti, S. Gould, P.K. Hansma, Control electronics for atomic force microscopy, Rev. Sci. Instrum. **59**, 836–839 (1988)
139. O. Wolter, T. Bayer, J. Greschner, Micromachined silicon sensors for scanning force microscopy, J. Vac. Sci. Technol. B **9**, 1353–1357 (1991)
140. E. Meyer, R. Overney, R. Luthi, D. Brodbeck, Friction force microscopy of mixed Langmuir–Blodgett films, Thin Solid Films **220**, 132–137 (1992)
141. H.J. Dai, J.H. Hafner, A.G. Rinzler, D.T. Colbert, R.E. Smalley, Nanotubes as nanoprobes in scanning probe microscopy, Nature **384**, 147–150 (1996)
142. J.H. Hafner, C.L. Cheung, A.T. Woolley, C.M. Lieber, Structural and functional imaging with carbon nanotube AFM probes, Prog. Biophys. Mol. Biol. **77**, 73–110 (2001)
143. G.S. Blackman, C.M. Mate, M.R. Philpott, Interaction forces of a sharp tungsten tip with molecular films on silicon surface, Phys. Rev. Lett. **65**, 2270–2273 (1990)
144. S.J. O'Shea, M.E. Welland, T. Rayment, Atomic force microscope study of boundary layer lubrication, Appl. Phys. Lett. **61**, 2240–2242 (1992)
145. J.P. Cleveland, S. Manne, D. Bocek, P.K. Hansma, A nondestructive method for determining the spring constant of cantilevers for scanning force microscopy, Rev. Sci. Instrum. **64**, 403–405 (1993)
146. D.W. Pohl, Some design criteria in STM, IBM J. Res. Dev. **30**, 417 (1986)
147. W.T. Thomson, M.D. Dahleh, *Theory of Vibration with Applications*, 5th edn. (Prentice Hall, Upper Saddle River 1998)
148. J. Colchero, Reibungskraftmikroskopie. Ph.D. Thesis (University of Konstanz, Konstanz 1993), in German

149. G.M. McClelland, R. Erlandsson, S. Chiang, Atomic force microscopy: General principles and a new implementation. In: *Review of Progress in Quantitative Nondestructive Evaluation*, Vol.6B, ed. by D.O. Thompson, D.E. Chimenti (Plenum, New York 1987) pp.1307–1314
150. Y.R. Shen, *The Principles of Nonlinear Optics* (Wiley, New York 1984)
151. T. Baumeister, S.L. Marks, *Standard Handbook for Mechanical Engineers*, 7th edn. (McGraw-Hill, New York 1967)
152. J. Colchero, O. Marti, H. Bielefeldt, J. Mlynek, Scanning force and friction microscopy, Phys. Status Solidi (a) **131**, 73–75 (1991)
153. R. Young, J. Ward, F. Scire, Observation of metal-vacuum-metal tunneling, field emission, and the transition region, Phys. Rev. Lett. **27**, 922 (1971)
154. R. Young, J. Ward, F. Scire, The topographiner: An instrument for measuring surface microtopography, Rev. Sci. Instrum. **43**, 999 (1972)
155. C. Gerber, O. Marti, Magnetostrictive positioner, IBM Tech. Discl. Bull. **27**, 6373 (1985)
156. R. Garcìa Cantù, M.A. Huerta Garnica, Long-scan imaging by STM, J. Vac. Sci. Technol. A **8**, 354 (1990)
157. C.J. Chen, In situ testing and calibration of tube piezoelectric scanners, Ultramicroscopy **42–44**, 1653–1658 (1992)
158. R.G. Carr, Finite element analysis of PZT tube scanner motion for scanning tunnelling microscopy, J. Microsc. **152**, 379–385 (1988)
159. C.J. Chen, Electromechanical deflections of piezoelectric tubes with quartered electrodes, Appl. Phys. Lett. **60**, 132 (1992)
160. N. Libioulle, A. Ronda, M. Taborelli, J.M. Gilles, Deformations and nonlinearity in scanning tunneling microscope images, J. Vac. Sci. Technol. B **9**, 655–658 (1991)
161. E.P. Stoll, Restoration of STM images distorted by time-dependent piezo driver aftereffects, Ultramicroscopy **42–44**, 1585–1589 (1991)
162. R. Durselen, U. Grunewald, W. Preuss, Calibration and applications of a high precision piezo scanner for nanometrology, Scanning **17**, 91–96 (1995)
163. J. Fu, In situ testing and calibrating of Z-piezo of an atomic force microscope, Rev. Sci. Instrum. **66**, 3785–3788 (1995)
164. R.C. Barrett, C.F. Quate, Optical scan-correction system applied to atomic force microscopy, Rev. Sci. Instrum. **62**, 1393 (1991)
165. R. Toledo-Crow, P.C. Yang, Y. Chen, M. Vaez-Iravani, Near-field differential scanning optical microscope with atomic force regulation, Appl. Phys. Lett. **60**, 2957–2959 (1992)
166. J.E. Griffith, G.L. Miller, C.A. Green, A scanning tunneling microscope with a capacitance-based position monitor, J. Vac. Sci. Technol. B **8**, 2023–2027 (1990)
167. A.E. Holman, C.D. Laman, P.M.L.O. Scholte, W.C. Heerens, F. Tuinstra, A calibrated scanning tunneling microscope equipped with capacitive sensors, Rev. Sci. Instrum. **67**, 2274–2280 (1996)

http://www.springer.com/978-3-642-15282-5

Nanotribology and Nanomechanics I
Measurement Techniques and Nanomechanics
Bhushan, B. (Ed.)
2011, XVIII, 623 p., Hardcover
ISBN: 978-3-642-15282-5